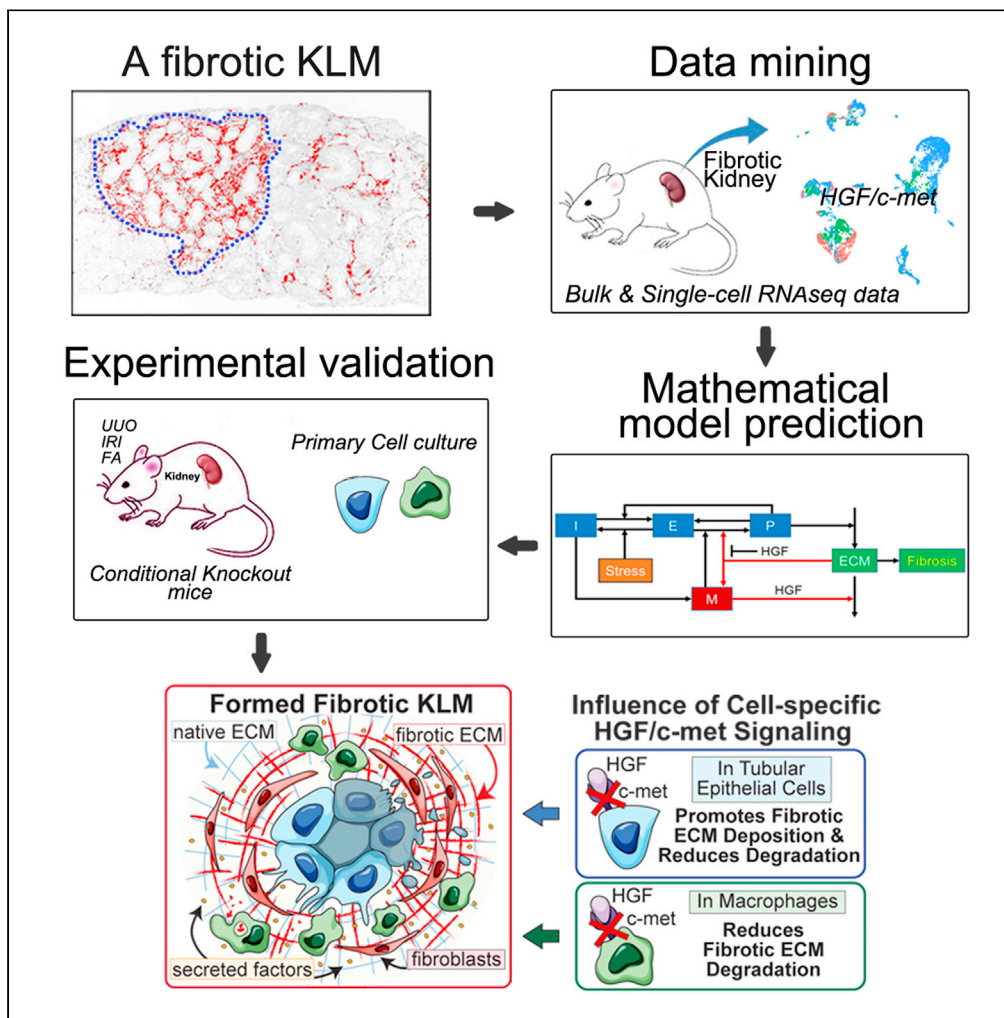# iScience

Article

The hepatocyte growth factor/c-met pathway is a key determinant of the fibrotic kidney local microenvironment

Haiyan Fu, Yuan Gui, Silvia Liu, ..., Xiao-Jun Tian, Youhua Liu, Dong Zhou

xiaojun.tian@asu.edu (X.-J.T.)
yhliu@pitt.edu (Y.L.)
dzhou@uchc.edu (D.Z.)

Highlights

A fibrotic kidney local microenvironment (KLM) is focal and segmental

C-met is more enriched in the distal tubule and collecting duct than in macrophages

Loss of c-met in tubular cells causes superior quick responses to simulated injury

HGF/c-met pathway determines the characteristics of a formed fibrotic KLM

Article

The hepatocyte growth factor/c-met pathway is a key determinant of the fibrotic kidney local microenvironment

Haiyan Fu,[1,2,9] Yuan Gui,[3,9] Silvia Liu,[1,9] Yuanyuan Wang,[1] Sheldon Ira Bastacky,[1] Yi Qiao,[4] Rong Zhang,[5] Christopher Bonin,[6] Geneva Hargis,[6] Yanbao Yu,[7] Donald L. Kreutzer,[4] Partha Sarathi Biswas,[8] Yanjiao Zhou,[6] Yanlin Wang,[3] Xiao-Jun Tian,[5,*] Youhua Liu,[1,*] and Dong Zhou[3,10,*]

SUMMARY

The kidney local microenvironment (KLM) plays a critical role in the pathogenesis of kidney fibrosis. However, the composition and regulation of a fibrotic KLM remain unclear. Through a multidisciplinary approach, we investigated the roles of the hepatocyte growth factor/c-met signaling pathway in regulating KLM formation in various chronic kidney disease (CKD) models. We performed a retrospective analysis of single-cell RNA sequencing data and determined that tubular epithelial cells and macrophages are two major cell populations in a fibrotic kidney. We then created a mathematical model that predicted loss of c-met in tubular cells would cause greater responses to injury than loss of c-met in macrophages. By generating c-met conditional knockout mice, we validated that loss of c-met influences epithelial plasticity, myofibroblast activation, and extracellular matrix synthesis/degradation, which ultimately determined the characteristics of the fibrotic KLM. Our findings open the possibility of designing effective therapeutic strategies to retard CKD.

INTRODUCTION

As the final outcome of chronic kidney disease (CKD), renal fibrosis is clinically described as inevitable, irreversible, and refractory (Duffield, 2014; Ruiz-Ortega et al., 2020). Over the years, substantial studies have deepened our understanding of renal fibrosis pathogenesis by interpreting the behavioral changes of resident or infiltrated cells and corroborating the participation of countless secreted factors in diseased kidneys at multiple biological dimensions (Kramann et al., 2015; Wen et al., 2019; Yang et al., 2010; Zhou et al., 2017). Technological advances along with unbiased evidence from high-throughput analyses have reilluminated the concept of the "kidney local microenvironment" (KLM) that may fully illustrate the pathologic changes of CKD (Conway et al., 2020; Kuppe et al., 2021; Park et al., 2018; Wu et al., 2019, 2020).

A KLM in healthy individuals is composed of mixtures of kidney cells that cooperate to maintain tissue integrity. In CKD, a disease-perpetuating KLM is formed and becomes a hallmark of the disease. Under fibrotic circumstances, the pathologic KLM surrounding a diseased spot is more than merely a static nest on which injured cells rest, but an active "communicator" that controls the balance of extracellular matrix (ECM) synthesis and degradation (Prunotto and Moll, 2011). Specific to renal tubulointerstitial injury, aberrantly activated fibroblasts, infiltrated inflammatory cells, and relentlessly deposited ECM are key constituents of the fibrotic site (Feng et al., 2018; Fu et al., 2017; Perry et al., 2019; Ren et al., 2019). Emerging data demonstrate that renal epithelial cells direct fibrotic biology of CKD, rather than being victims or bystanders. Amid the formation of a fibrotic KLM, epithelial cells communicate with resident fibroblasts or infiltrated cells to carry out so-called maladaptive repair (Maarouf et al., 2016; Zhou et al., 2014, 2017). In the meantime, some injured epithelial cells exhibit mesenchymal characteristics after undergoing partial epithelial-mesenchymal transition (EMT), or epithelial plasticity (Chang-Panesso and Humphreys, 2017; Liu, 2010; Lovisa et al., 2015; Nieto, 2013). Although each cellular component is a functional single entity in the fibrotic KLM, the dynamics of the network within cellular and non-cellular compartments remain ambiguous.

[1]Department of Pathology, University of Pittsburgh School of Medicine, Pittsburgh, PA 15261, USA

[2]State Key Laboratory of Organ Failure Research, National Clinical Research Center of Kidney Disease, Division of Nephrology, Nanfang Hospital, Southern Medical University, Guangzhou 510515, China

[3]Division of Nephrology, Department of Medicine, University of Connecticut School of Medicine, Farmington, CT 06030, USA

[4]Department of Surgery, University of Connecticut School of Medicine, Farmington, CT 06030, USA

[5]School of Biological and Health Systems Engineering, Arizona State University, Tempe, AZ 85287, USA

[6]Department of Medicine, University of Connecticut School of Medicine, Farmington, CT 06030, USA

[7]Department of Chemistry and Biochemistry, University of Delaware, Newark, DE 19716, USA

[8]Division of Rheumatology and Clinical Immunology, University of Pittsburgh School of Medicine, Pittsburgh, PA 15261, USA

[9]These authors contributed equally

[10]Lead contact

*Correspondence:
xiaojun.tian@asu.edu
(X.-J.T.), yhliu@pitt.edu (Y.L.),
dzhou@uchc.edu (D.Z.)

https://doi.org/10.1016/j.isci.2021.103112

A

	Non-tumor Control	FSGS	IgAN	MN
α-SMA				
Blue Channel				
Vimentin				
Blue Channel				
CD68				
Blue Channel				
CD14				
Blue Channel				

B α-SMA+ Area (%) p<0.01 p<0.01 p<0.01 NC FSGS IgAN MN

C Vimentin+ Area (%) p<0.01 p<0.01 p<0.01 NC FSGS IgAN MN

D CD68+ Area (%) p<0.01 p<0.01 p<0.01 NC FSGS IgAN MN

E CD14+ Area (%) p<0.01 p<0.01 p<0.01 NC FSGS IgAN MN
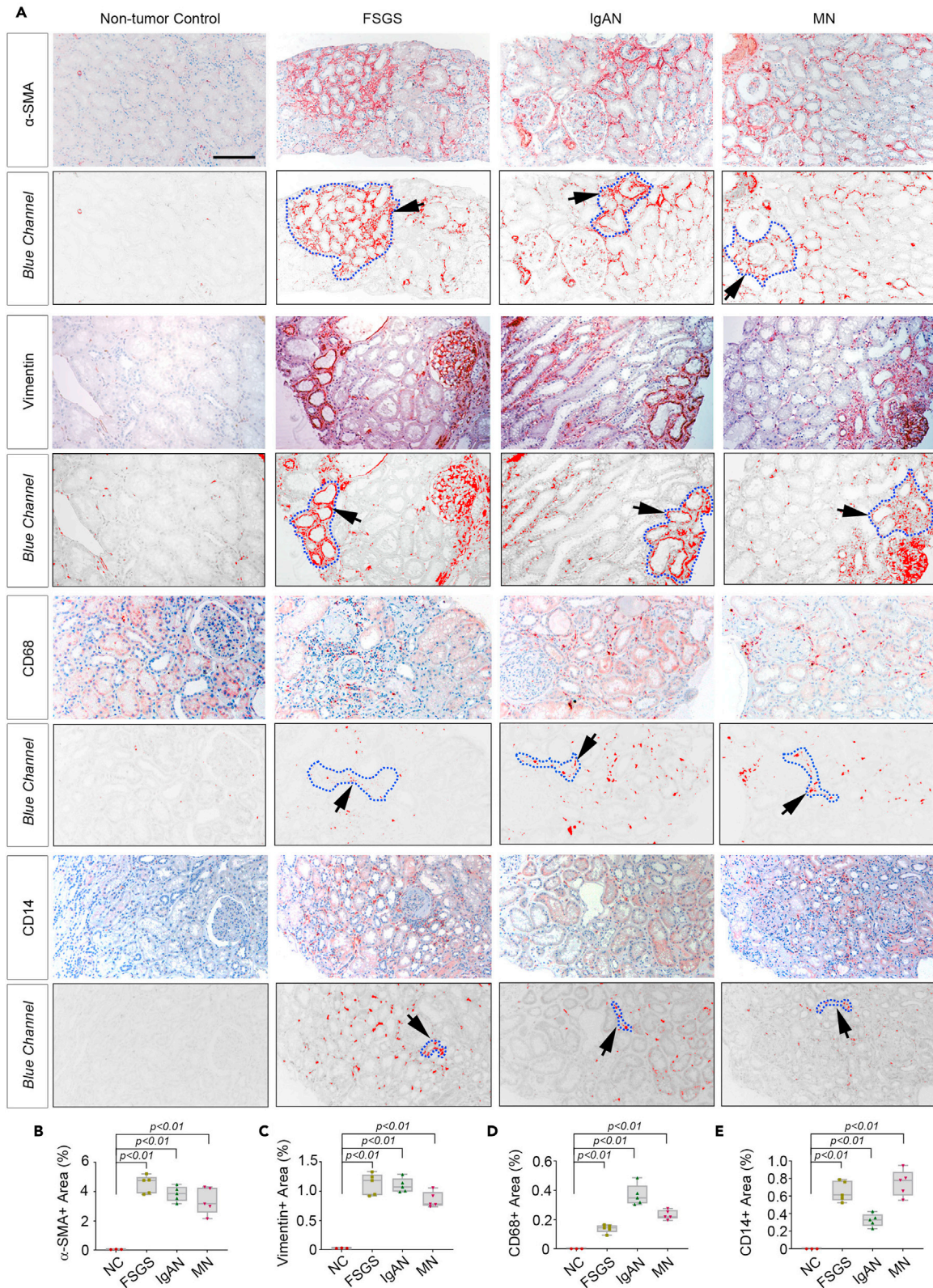
Figure 1. The characteristics of KLM in human diseased kidneys

(A) Representative immunohistochemical staining images showing the patterns of α-SMA, vimentin, CD68, and CD14 expression in non-tumor normal human kidney (n = 3), and kidney biopsy specimens from patients diagnosed with focal segmental glomerulosclerosis (FSGS), IgA nephropathy (IgAN), and membrane nephropathy (MN). Five cases were employed *per* diagnosis. The images in the blue channel were used to identify the fibrotic area (blue outline). Arrows indicated positive staining. Scale bar, 50 μm. Quantitative data are presented (B–E). Data are represented as mean ± SEM. Statistical significance was assessed by one-way ANOVA, followed by the Student-Newman-Keuls test.

Hepatocyte growth factor (HGF) is a mesenchymal-derived, multifunctional protein that prevents kidney fibrogenesis (Liu, 2002). The biological activities of HGF are mediated mainly by the c-met receptor expressed on most types of kidney cells (Matsumoto and Nakamura, 2001). HGF/c-met signaling is tightly linked to multiple cellular processes, including proliferation, survival, motility, angiogenesis, invasion, and metastasis (Noriega-Guerra and Freitas, 2018). Amid the development of renal fibrosis, HGF can interact with matricellular protein/protease to either sequester HGF away from the cell surface or degrade the synthesized matrix to regulate ECM turnover, by which determines the kidney fate after CKD. However, the roles of HGF in building the fibrotic KLM have not been well characterized. Novel, multidisciplinary studies are necessary to unveil the mysteries of this comprehensive system.

In this study, we investigated the formation of fibrotic KLM in human CKD patients. Through data mining, mathematical model construction, and conditional knockout mice, we specified the characteristics and functions of tubule- and macrophage-derived c-met in fibrotic KLM formation. Our study provides a new angle to systemically explore the unrecognized mechanisms of kidney fibrosis.

RESULTS

The characteristics of KLM in human diseased kidneys

To establish the clinical relevance of fibrotic microenvironment formation in the pathogenesis of human CKD, we first specified the features of KLM in kidney biopsy specimens from CKD patients with different etiologies (diagnosis and demographic data are shown in Table S1). As illustrated in Figure 1, the classic marker of myofibroblasts α-smooth muscle actin (α-SMA) was significantly activated in all enrolled patients diagnosed with focal segmental glomerulosclerosis (FSGS), IgA nephropathy (IgAN), and membranous nephropathy (MN), compared with non-tumor normal human kidneys. Interestingly, α-SMA-associated fibrotic lesions were not homogeneous throughout the kidney (Figure 1A). The size of this fibrotic area appeared to be associated with the severity of CKD in each patient.

To further describe the features of KLM, we analyzed the expression of vimentin, a well-known type III intermediate filament protein, and found that it was expressed in mesenchymal cells of the kidney biopsy specimens. Vimentin was predominantly localized to the interstitium and renal tubules. The vimentin + cell distribution in diseased kidneys was focal, although vimentin + cell density was much lower than α-SMA. These vimentin + fibroblasts and tubular cells produce a large amount of ECM components at certain foci, which serve as the backbone of a fibrotic KLM. Through partial EMT or epithelial plasticity, vimentin + tubular cells possess the mesenchymal characteristic that promotes active involvement in fibrotic KLM formation (Figure 1A). Furthermore, CD68, a protein highly expressed by circulating monocytes/tissue macrophages, and CD14, a human protein made mostly by macrophages were detected surrounding the fibrotic focal sites in human diseased kidneys (Figure 1A). The quantified expression levels of α-SMA, vimentin, CD68, and CD14 are presented in Figures 1B–1E. Together, these data indicate that myofibroblasts, vimentin + fibroblasts, tubular epithelial cells, and macrophages occupy the fibrotic KLM lesions in chronically injured kidneys.

HGF/c-met expression in tubular epithelial cells and macrophages may mediate fibrotic KLM formation

Cellular components and secreted soluble factors are necessary for fibrotic KLM formation. However, our understanding of the pathogenesis of CKD is largely limited due to incomplete molecular characterizations of the various types of cells responsible for kidney homeostasis (Park et al., 2018). We previously reported HGF is a mesenchymal-derived potent mitogen that inhibits kidney fibrogenesis by binding to its receptor c-met (Yang et al., 2003). To further delineate the cell specificity of HGF/c-met expression, we analyzed publicly available bulk RNA-seq and single-cell RNA-seq data. To investigate the overall expression of *HGF* and *c-met* in the whole kidney, we analyzed RNA expression data from a study where fibrosis was induced in mice using unilateral ureteral obstruction (UUO) (or sham control), RNA was extracted 5 and
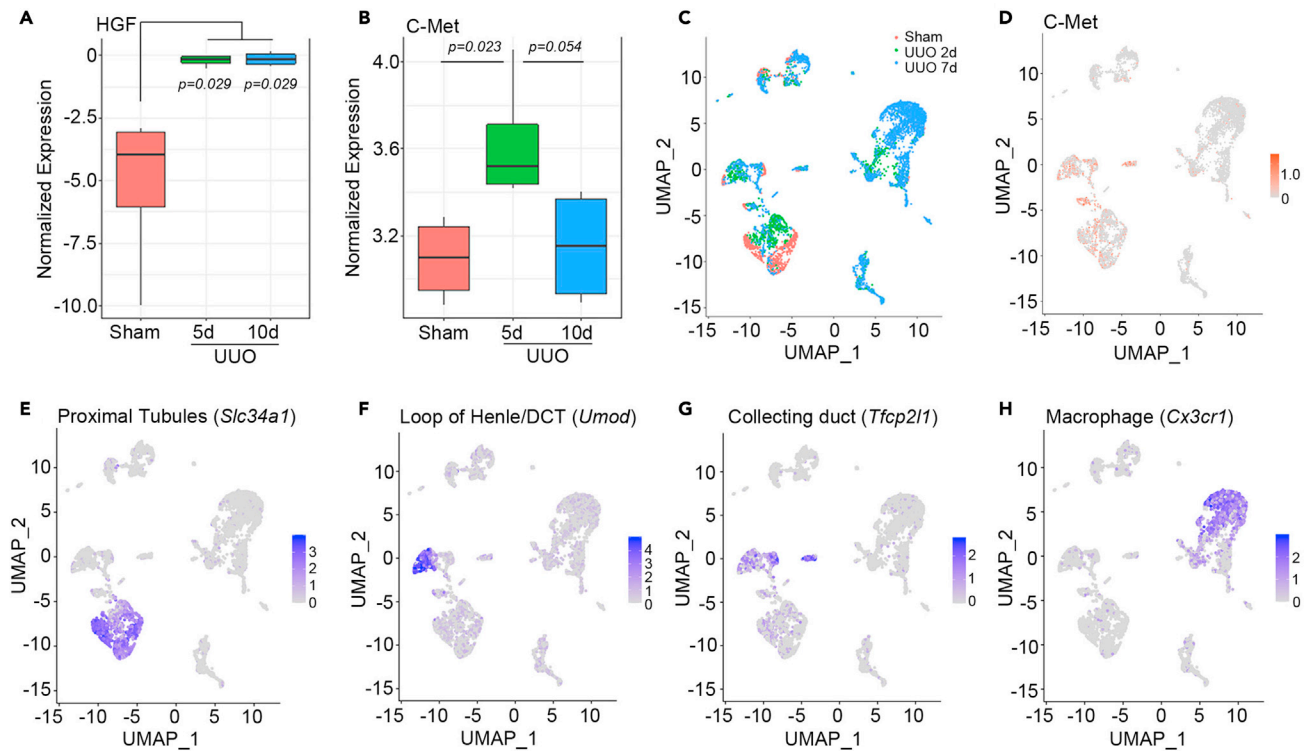
Figure 2. HGF/c-met expression in tubular epithelial cells and macrophages may mediate fibrotic KLM formation

(A and B) Bulk RNA-seq data (Database: GSE125015) showing (A) normalized HGF and (B) c-met expression in whole male mouse kidneys subjected to sham surgery (control) or UUO after 5 and 10 days. Data are represented as mean ± SEM. Statistical significance was assessed by one-way ANOVA, followed by the Student-Newman-Keuls test.

(C–H) Single-cell RNA-seq data (Database: GSE140023) were visualized by UMAP algorithm, where UMAP_1 and UMPA_2 represent the two reduced dimensions and each dot in the figure indicates one cell. (C) Kidney single cells clustered by sham control or 2 days and 7 days after UUO. At the single-cell level, (D) c-met expression was localized in specific subpopulations of kidney cells. Expression of Slc34a1, Umod, Tfcp2l1, and Cx3cr1 identified a subpopulation of kidney tubular cells (E-G) and macrophages (H).

10 days later, and RNA was sequenced with RNA-seq (Database: GSE125015) (Wu et al., 2020). Our analysis revealed differential expression of both *HGF* and *c-met* genes. In both male and female mouse kidneys, *HGF* had high expression at 5 and 10 days after UUO surgery, compared with the sham control (Figure 2A and S1A). Intriguingly, after UUO, the HGF receptor *c-met* showed high expression on day 5 but low expression on day 10 if compared with its levels on day 5 in male mice (Figure 2B). In contrast, female mice exhibited higher *c-met* levels in the obstructed kidneys on day 10 than day 5 (Figure S1B).

We then explored *c-met* expression further at the single-cell level by analyzing single-cell RNA-seq (scRNA-seq) data from a similar UUO male mouse study where scRNA-seq was performed 2 and 7 days after surgery (Database: GSE140023) (Conway et al., 2020). Gene expression in kidney cells was clustered by sham and 2 days or 7 days after UUO injury (Figure 2C). Figure 2D presents the population of c-met+ cells in the whole kidney single-cell pool. We found that tubular epithelial cells and macrophages are two major cellular populations in the obstructed kidney (Figures 2E–2H). In the fibrotic kidneys, the ratio of *c-met+: c-met-* cells was high in the loop of Henle/distal convoluted tubules (DCT, labeled by *Umod* gene marker) and collecting ducts (labeled by *Tfcp2l1* gene marker), but relatively low in the macrophage population (labeled by *Cx3cr1* gene marker). Collectively, through public data mining, we found that tubular epithelial cells, macrophages, and the HGF/c-met pathway are potentially involved in building the fibrotic KLM.

Mathematical modeling predicts tubular epithelial cells and macrophages accelerate fibrotic KLM formation

Our analysis of public RNA-seq data determined that *c-met* is specifically expressed in the loop of Henle/distal convoluted tubules, collecting ducts, and some macrophages at the single-cell level in a UUO kidney
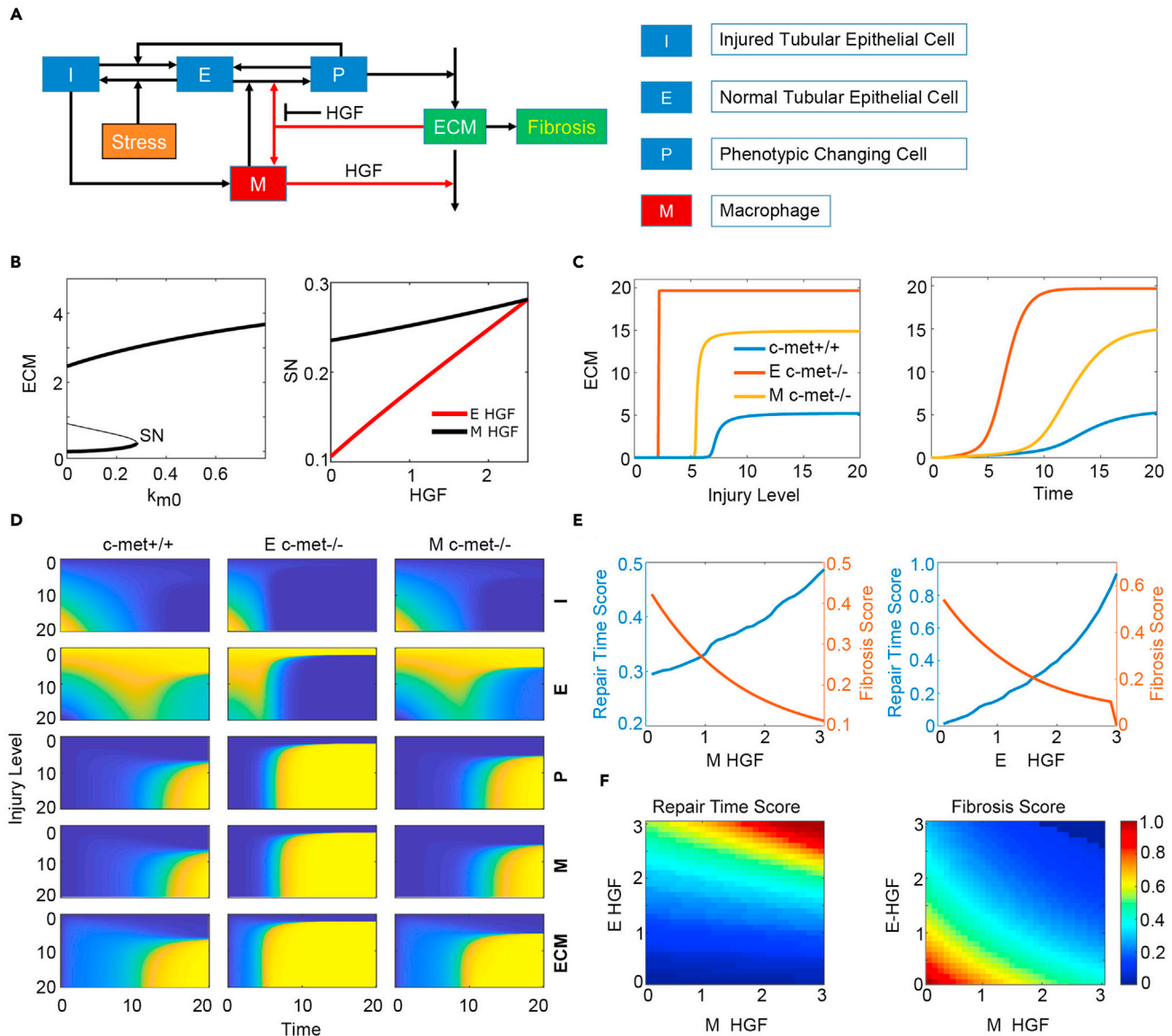
Figure 3. Mathematical modeling predicts tubular epithelial cells and macrophages accelerate fibrotic KLM formation

(A) Diagram of the cell-cell communication model for renal fibrosis.

(B) Bifurcation diagram of ECM level with respect to macrophage activation rate (k_{m0}) (Left). The dependence of the fibrosis threshold (SN) on the levels of epithelial-HGF (E-HGF) and macrophage-HGF (M-HGF) (Right).

(C) The dose-response curve of ECM levels with respect to the injury level under either E-HGF c-met−/− (orange line) or M-HGF c-met−/− (yellow line) knockdown (Left). The WT c-met+/+ (blue line) is shown as a control. The temporal dynamics of ECM level under normal, E-HGF knockdown, and M-HGF knockdown conditions (Right). The injury level is fixed as high.

(D) The temporal dynamics of the system variables in the space of the injury levels under normal (c-met+/+), E-HGF knockdown, and M-HGF knockdown conditions.

(E) The dependence of the repair and fibrosis scores on M-HGF (Left) and E-HGF (Right).

(F) Phase diagram of repair and fibrosis scores in the space of M-HGF and E-HGF.

fibrosis model. Therefore, to further understand the exact roles of HGF/c-met signaling in tubular epithelial cells (E) and macrophages (M) in fibrotic KLM formation, we developed a mathematical model by considering tubular epithelial cells and their phenotypic transition, macrophage activation, ECM accumulation, HGF, and the communications among these elements (Figure 3A). First, we conducted a steady-state analysis. We found that the threshold of kidney fibrosis was markedly increased along with the changes of HGF levels both in tubular epithelial cells and macrophages (Figure 3B). Knockdown of HGF/c-met signaling in either tubular epithelial cells or macrophages accelerated excessive ECM accumulation. Intriguingly, the
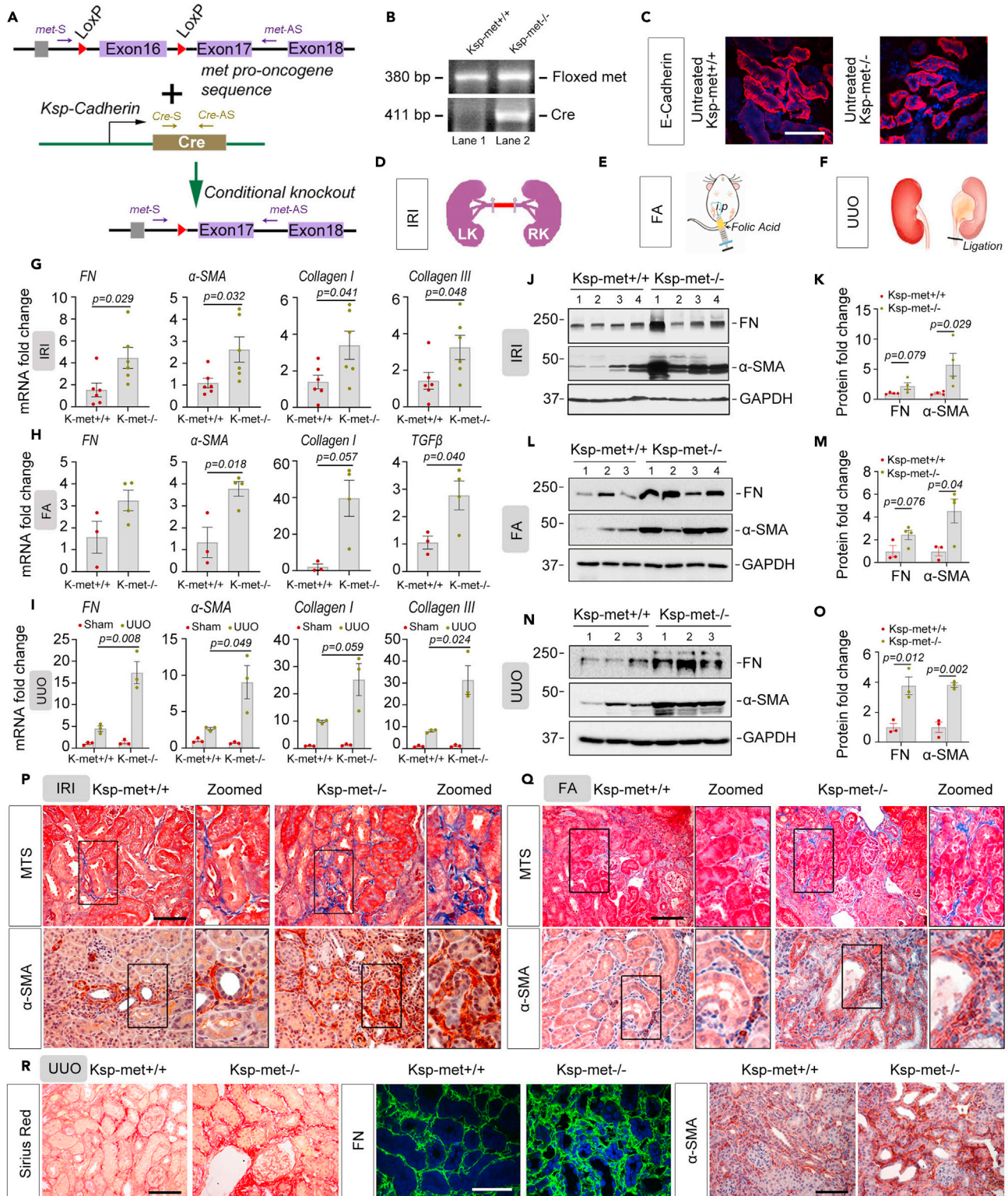
Figure 4. Tubular-specific ablation of c-met exacerbates fibroblast activation and ECM synthesis

(A) Schematic diagram depicting the generation of tubular epithelial cell-specific c-met conditional knockout mice.

(B) Mice genotyping analyses for the control mice used in this study (genotype: c-met$^{fl/fl}$, lane 1), designated as Ksp-met+/+, while lane 2 demonstrates the genotyping of the tubular c-met knockout mice (genotype: c-met$^{fl/fl}$, Cre), designated as Ksp-met−/−.

Figure 4. Continued

(C) Immunofluorescence staining showing E-cadherin expression in the untreated Ksp-met+/+ and Ksp-met−/− mouse kidneys. Scale bar, 50 μm.

(D–F) Diagrams representing the strategies for the surgeries or treatment in mice, IRI (10 days), FA (60 days), and UUO (7 days).

(G–I) qPCR analyses revealed the mRNA abundance of *FN*, *α-SMA*, *type I collagen*, *type III collagen*, or *TGF-β* in Ksp-met+/+ and Ksp-met−/− mice kidneys after IRI (G), FA (H), and UUO (I). n = 3–6.

(J–O) Western blot analyses demonstrated FN and α-SMA protein expression in Ksp-met+/+ and Ksp-met−/− mice kidneys after IRI (J), FA (L), and UUO (N), and quantified data (K, M, and O). Dots indicate individual animals within each group. n = 3–4.

(P–R) Representative micrographs for Masson's trichrome, Sirius red, α-SMA, and FN staining in kidneys from Ksp-met+/+ and Ksp-met−/− mice after IRI, FA, and UUO. n = 3–4. Scale bar, 50 μm. IRI, ischemia-reperfusion injury; FA, folic acid injection; UUO, unilateral ureteral obstruction. Data are represented as mean ± SEM. Statistical significance was assessed using a two-tailed Student's t-test or the Rank Sum Test if data failed in normality test or two-way ANOVA, followed by the Student-Newman-Keuls test.

threshold of fibrosis was much more sensitive to HGF/c-met abundance in tubular epithelial cells than HGF/c-met abundance in macrophages (Figure 3B). We also performed sensitivity analysis, which shows that 15% increase or decrease of each parameter did change the threshold of fibrosis under wild type (WT), E-HGF/c-met−/−, and M-HGF/c-met−/− (Figures S2A–S2C). However, the fibrosis threshold decreased in both knockdown cases as demonstrated by the ratio of fibrosis threshold in the knockdown cases to that in the WT case ($SN^{E\ c\text{-}met\text{-}/\text{-}}/SN^{WT}$ and $SN^{M\ c\text{-}met\text{-}/\text{-}}/SN^{WT}$) which was always smaller than 1 (Figures S2D and S2E). This confirms the prediction that both tubular epithelial cells and macrophages accelerate fibrotic KLM formation. We noted that $SN^{E\ c\text{-}met\text{-}/\text{-}}/SN^{WT}$ is always much smaller than $SN^{M\ c\text{-}met\text{-}/\text{-}}/SN^{WT}$ (Figures S2D and S2E), confirming that the threshold of fibrosis was much more sensitive to HGF/c-met abundance in tubular epithelial cells than in macrophages. This finding was further confirmed in the dose-response of ECM accumulation under different injury levels (Figure 3C, Left). Furthermore, through a head-to-head comparison, ECM accumulation was significantly accelerated if loss of HGF/c-met occurred in tubular epithelial cells than if deletion occurred in macrophages (Figure 3C, Right). In Figure 3D, the different rates of ECM accumulation were further demonstrated in various tubular epithelial cells, macrophages, and epithelial phenotypic transition cells at multiple levels of injury. It was clear that when c-met is knocked down in epithelial cells, the activated epithelial cells undergo rapid phenotypic transitions, and macrophage activation is accelerated, leading to greater renal fibrosis. In other words, there was a trade-off for renal damage repair and fibrosis in the current system (Tian et al., 2020), which is consistent with the HGF signaling changes in both tubular cells and macrophages. The repair score was increased while the fibrosis score was certainly decreased along with the changes of HGF levels, as shown in Figure 3E. When examining the effects of HGF signaling in tubular epithelial cells and macrophages, the repair score was maximal when both epithelial cells and macrophages expressed a high level of HGF while the fibrosis score was maximal when both cell types expressed no HGF (Figure 3F). Thus, the levels of HGF signaling in both tubular epithelial cells and macrophages were well balanced according to this trade-off. Perturbations of HGF signaling in different kidney cells are believed to lead to the heterogeneous nature of the fibrotic KLM.

Tubular-specific ablation of c-met exacerbated fibroblast activation and excessive ECM synthesis

Since c-met is enriched in the loop of Henle/distal convoluted tubules and collecting ducts in the fibrotic kidney at the single-cell level, and to validate the prediction produced by the mathematical model, we first generated conditional knockout mice using the Cre-LoxP system where the c-met receptor was specifically deleted in the loop of Henle/distal convoluted tubules and collecting ducts (Figure 4A and Figures S3A–S3C). Homozygous c-met-floxed mice were mated with the transgenic mice expressing Cre recombinase under the control of the Ksp-cadherin promoter to create tubule-specific c-met conditional knockout mice (designated as Ksp-met−/−; Figure 4B, lane 2). Age and sex-matched c-met-floxed littermates (designated as Ksp-c-met+/+) were used as controls (Figure 4B, lane 1). Mice with tubule-specific deletion of c-met (Ksp-met−/−) were phenotypically normal. Immunostaining showed that there was no difference in E-cadherin, fibronectin, α-SMA, and type I collagen expression between Ksp-met+/+ and Ksp-met−/− mice under physiological conditions (Figures 4C and S3D). To enhance the reproducibility of our analyses, a total of 23 mice were subjected to three well-characterized models of renal fibrosis induced by renal ischemic-reperfusion injury (IRI, Figure 4D), folic acid (FA) administration (Figure 4E), and UUO (Figure 4F). Considering there was no appreciable abnormality in kidney tubule integrity of Ksp-met−/− mice compared with Ksp-met+/+ mice (Zhou et al., 2013), to minimize the animal number used in a single study, we did not include sham control groups in the FA and IRI models.
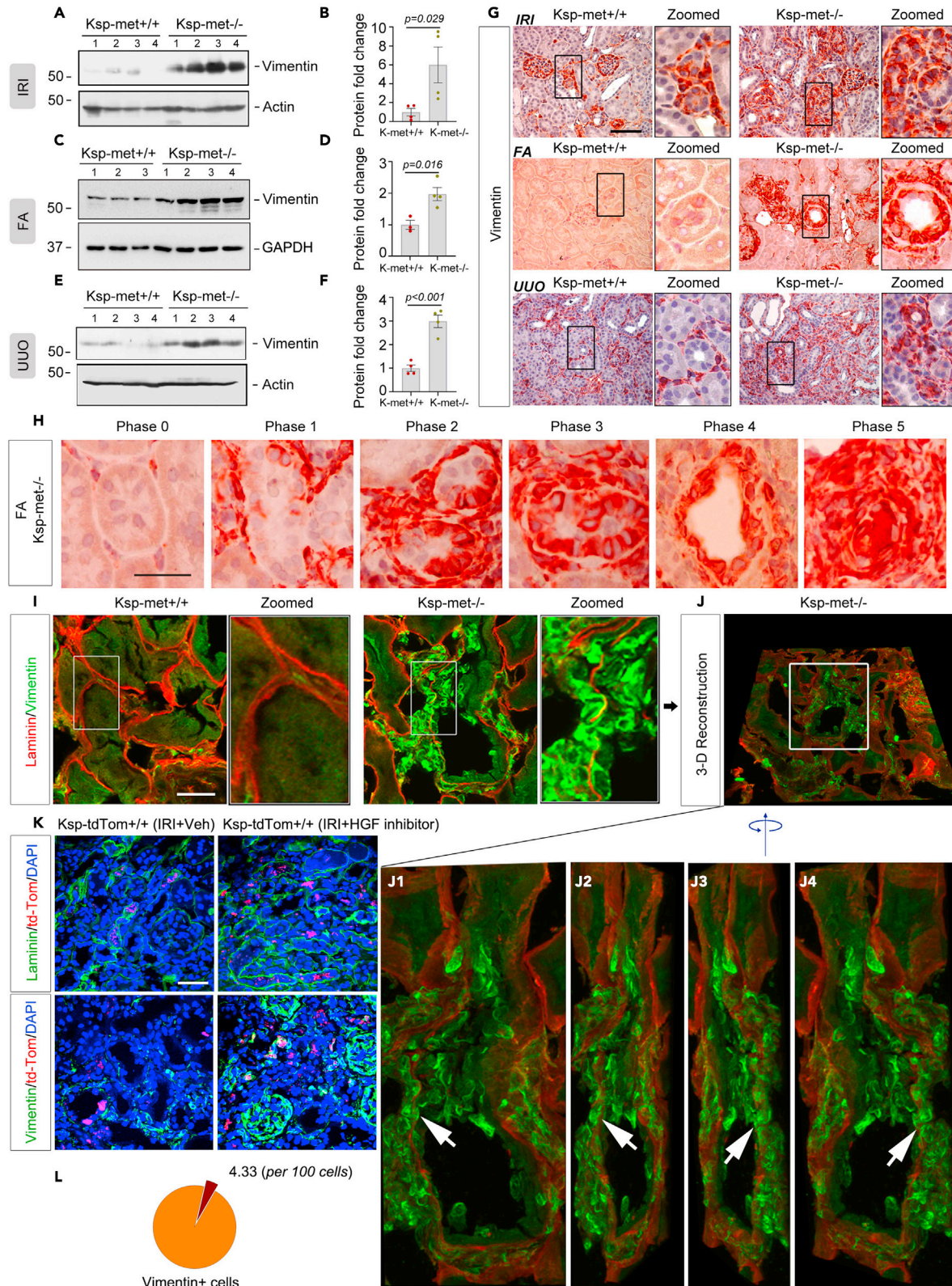
Figure 5. Specific deletion of c-met in tubules influences epithelial plasticity towards kidney fibrosis

(A–F) Western blot analyses demonstrated vimentin expression in Ksp-met+/+ and Ksp-met−/− mice kidneys after IRI (A), FA (C), and UUO (E). Quantitative data presented in B, D, and F, respectively. Dots indicate individual animals within each group. n = 3–4. Data are represented as mean ± SEM. Statistical significance was assessed using a two-tailed Student's t-test.

(G) Immunohistochemical staining showing the distributions of vimentin in Ksp-met+/+ and Ksp-met−/− mice kidneys after IRI, FA, and UUO. Scale bar, 50 μm.

(H) Representative images showing the induction of vimentin in diseased tubules after FA. Scale bar, 25 μm.

(I and J) Immunofluorescence staining for vimentin expression in kidneys after FA. 3-D reconstruction images (J, J1–J4). Scale bar, 25 μm.

(K) Representative micrographs showing the localization of td-Tomato + cells by co-staining with laminin and vimentin in Ksp-tdTom−/− mice treated with HGF inhibitor or vehicle at 10 days after IRI. Scale bar, 25 μm.

(L) Pie chart of vimentin+/td-Tomato+ tubular cells in fibrotic kidneys after IRI. IRI, ischemia-reperfusion injury; FA, folic acid injection; UUO, unilateral ureteral obstruction.

After IRI at 10 days, mRNA expression levels of the fibrosis-related genes *fibronectin, α-SMA, type I collagen*, and *type III collagen* were significantly increased in the Ksp-met−/− mice diseased kidneys compared to Ksp-met+/+ mice (Figure 4G). Similarly, these genes were consistently induced in Ksp-met−/− mice kidneys 60 days after FA administration and 7 days after UUO, compared with Ksp-met+/+ controls (Figures 4H and 4I). Western blot analyses demonstrated markedly elevated expression of fibronectin and α-SMA proteins in the diseased kidney of Ksp-met−/− mice in all three models, compared with their littermate controls (Figures 4J–4O). Furthermore, by immunostaining, Masson's tri-chrome staining (MTS), and Sirius red staining, we identified significantly activated α-SMA + myofibroblasts and collagen focal deposition in the fibrotic kidneys of Ksp-met−/− mice in all three models, compared to the Ksp-met+/+ controls (Figures 4P–4R, S4A–S4F). Meanwhile, 60 days after FA injection, loss of tubular c-met resulted in kidney dysfunction, increased infiltration of F4/80 + macrophages in the diseased kidneys, and mRNA upregulation of secreted cyto-chemokines, such as monocyte chemoattractant protein-1 (MCP-1), regulated on activation normal T cell expressed and secreted (RANTES), and tumor necrosis factor-α (TNF-α), compared with Ksp-met+/+ controls (Figures S5A–S5C). In addition, in cultured human kidney proximal tubular cells (HKC-8), the induction of α-SMA by transforming growth factor β1 (TGF-β1) was largely abolished after incubation with HGF recombinant protein, while it could be restored by inhibiting c-met activity (Figure S5D). Together, these data indicate that tubular c-met is a critical regulator of the formation of the multi-cellular components involved in comprehensive fibrotic KLM.

Loss of tubular c-met influenced epithelial cell plasticity towards fibrosis

Previously, we and others reported that HGF/c-met signaling plays an 'anti-EMT' role in renal fibrosis (Yang et al., 2005; Yu et al., 2009). However, EMT is a controversial topic in renal fibrogenesis (Kriz et al., 2011; Liu, 2010). Current evidence indicates that epithelial cell phenotypic transition undergoes partial EMT or epithelial plasticity rather than complete EMT (Saitoh, 2018), which poses a higher risk in driving kidney fibrosis (Lovisa et al., 2015, 2016; Sheng and Zhuang, 2020). The definition of 'epithelial plasticity' is that cells possess the ability to reversibly change their phenotype (Nieto, 2013). To refresh our understanding of the role of HGF/c-met in epithelial plasticity, we examined vimentin expression in fibrotic kidneys collected from the three CKD models. As shown in Figures 5A–5F, western blot analyses demonstrated marked induction of vimentin in fibrotic kidneys of Ksp-met−/− mice, compared with Ksp-met+/+ controls. We next sought to determine the localization of vimentin+ cells in the fibrotic kidneys. In all three CKD models, by immunohistochemical staining, we found a certain amount of vimentin+ tubular epithelial cells exhibited mesenchymal characteristics in Ksp-met−/− mice kidneys, compared with Ksp-met+/+ controls (Figure 5G, "Zoomed"; Figures S6A–S6C). In particular, we found that the distribution of vimentin+ tubular cells was scattered across the Ksp-c-met−/− mice kidneys in the FA model (Figure 5H). These vimentin+ epithelial cells could be classified as all 6 phases (0–5) even though they reside in a single fibrotic kidney, which reflects the spectrum of the phenotypic changes in tubules. Along with the increased number of vimentin+ cells in the diseased tubules, a number of cellular components start to migrate and noncellular components get recruited to the injured site to form irreversible structural changes. Of note, E-cadherin, a tubular epithelial cell adhesion molecule, was also largely diminished in the Ksp-met−/− mice fibrotic kidneys, compared with Ksp-met+/+ controls (Figure S6D).

To further delineate the localization of the vimentin+ tubular cells in fibrotic kidneys, we performed double immunostaining for vimentin (green) and a marker of the tubular base membrane, laminin (red), in kidneys after FA administration. From a 2-D perspective, the majority of vimentin+ tubular cells remained in their original locations after injury in Ksp-c-met−/− mice kidneys, although vimentin expression was significantly
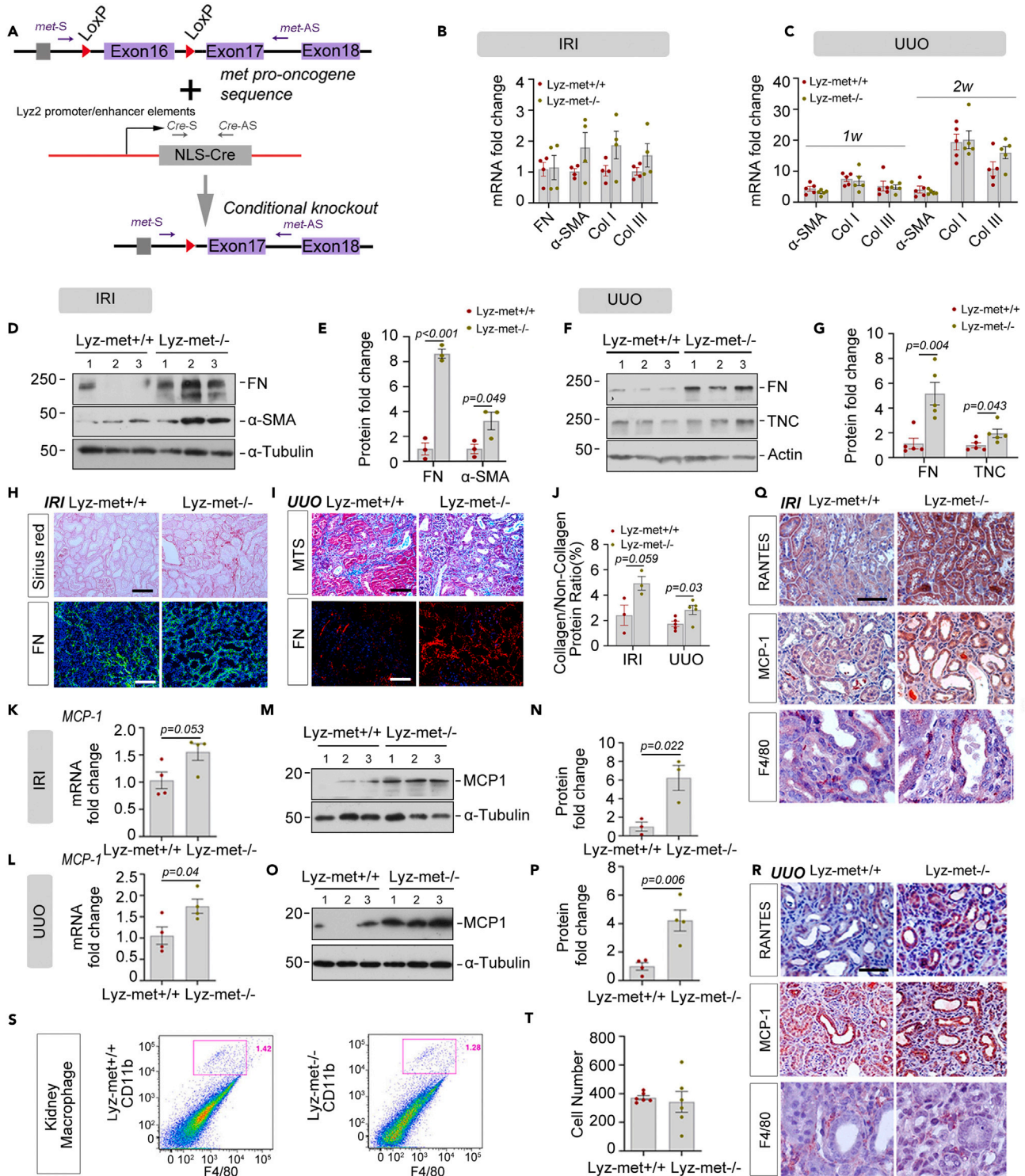
Figure 6. Macrophage-specific deletion of c-met enhances fibrosis but has little effect on extracellular matrix (ECM) synthesis

(A) Schematic diagram showing the generation of macrophage-specific c-met deletion mice.

(B and C) qPCR analyses of *FN, α-SMA, type I collagen*, and *type III collagen* mRNA in Lyz-met+/+ and Lyz-met−/− mice kidneys after IRI at 10 days and UUO at 7 (1 week [w]) and 14 days (2 w). n = 4–5.

(D–G) Western blot analyses of FN, α-SMA, and TNC protein expression in Lyz-met+/+ and Lyz-met−/− mice kidneys after IRI (D) and UUO (F). Quantification of protein expression for IRI (E) and UUO (G). Dots indicate individual animals within each group. n = 3–5.

Figure 6. Continued

(H and I) Representative micrographs for Sirius red, Masson's trichrome, and FN staining in Lyz-met+/+ and Lyz-met−/− mice kidneys after IRI and UUO, respectively. Scale bar, 50 μm.

(J) Bar graph of collagen/non-collagen ratios in Lyz-met+/+ and Lyz-met−/− mice kidneys after IRI and UUO, respectively. n = 3–5.

(K) qPCR analyses of *MCP-1* mRNA in Lyz-met+/+ and Lyz-met−/− kidneys after IRI. n = 4.

(L) qPCR analysis of *MCP-1* mRNA in Lyz-met+/+ and Lyz-met−/− mice kidneys after UUO. n = 4.

(M and N) Western blot analyses (M) and quantitative data (N) of MCP-1 protein expression in Lyz-met +/+ and Lyz-met −/− mice kidneys after IRI. Dots indicate individual animals within each group. n = 3.

(O and P) Western blot analyses (O) and quantitative data (P) demonstrating MCP-1 protein expression in Lyz-met+/+ and Lyz-met−/− mice kidneys after UUO. Dots indicate individual animals within each group. n = 4.

(Q and R) Representative images showing RANTES, MCP-1, and F4/80 expression in Lyz-met +/+ and Lyz-met−/− mice kidneys after UUO. Scale bar, 50 μm.

(S and T) FACS analysis revealed no significant difference in macrophage numbers from Lyz-met+/+ and Lyz-met−/− mice fibrotic kidneys after IRI at 10 days. n = 6. Data are represented as mean ± SEM. Statistical significance was assessed using a two-tailed Student's t-test.

increased (Figure 5I). By using a 3D reconstruction technique, we found very few vimentin+ tubular cells traversed into the interstitium through the interrupted tubular basement membrane (Figure 5J, 5J1–5J4). Consistently, by double staining with vimentin and E-cadherin, we also found that the majority of vimentin+ tubular cells remained inside the human diseased kidney tubules (Figure S7).

To quantify the number of cells undergoing epithelial plasticity in the fibrotic kidneys after HGF/c-met signaling blockade, we bred the Ksp-cadherin promoter Cre recombinase mouse line to the floxed-stopped tdTomato reporter strain and obtained mice expressing robust tdTomato fluorescence in the target tubular cells, as demonstrated by immunostaining with laminin (Figure 5K). The mice were then subjected to IRI for 10 days. On the 4th day after surgery, c-met inhibitor SU11274 was administrated *in vivo*. At 10 days after IRI, blockade of HGF/c-met signaling markedly aggravated serum creatinine compared with vehicle controls (Figure S8A). Western blot analyses demonstrated that induction of E-cadherin was largely abolished after c-met blockade, compared with vehicle controls (Figure S8B). By immunostaining with vimentin and E-cadherin (Figures 5K and S8C), we found that the overall ratio of vimentin+/tdTomato+ tubular cells was about 4.33 *per* 100 tdTomato+ cells in the injured kidneys after HGF/c-met signaling pathway blockade (Figure 5L). In particular, very few vimentin+/tdTomato+ cells detached from the tubule basement membrane and migrated to the interstitial compartment. Together, these results indicated loss of HGF/c-met signaling influences epithelial plasticity toward fibrosis.

Macrophage-specific deletion of c-met deteriorates fibrosis but has little effect on ECM synthesis

To fully understand the composition of the fibrotic KLM, we explored the roles of another essential cellular component of the KLM, macrophages. To this end, we used the Cre-LoxP system to create a c-met receptor macrophage-specific conditional knockout mouse (Figure 6A). The Cre recombinase was under the control of the endogenous lysozyme 2 gene promoter/enhancer elements. The results of the genotyping assay for the conditional knockout mice (designated as Lyz-met−/−), and their littermates (designated as Lyz-met+/+) are presented in Figure S9A. Immunofluorescence staining further confirmed that c-met was effectively deleted in mouse macrophages (Figure S9B). These mice were then subjected to IRI and UUO, respectively.

At 10 days after IRI and 7 days after UUO, we examined the mRNA expression of *fibronectin*, *α-SMA*, *type I collagen*, and *type III collagen* in the fibrotic kidneys. Surprisingly, little differences were observed between Lyz-met+/+ and Lyz-met−/− mice (Figures 6B and 6C). Serum creatinine levels were markedly induced in Lyz-met−/− mice after IRI, if compared with Lyz-met+/+ (Figure S9C). Considering that our mathematical model predicted that loss of c-met in macrophages would cause much less sensitive responses in producing pathologic ECM compared with tubular cells, we used the Lyz-met−/− mice and controls to reconstruct the second batch of UUO mice with a prolonged duration to 2 weeks. Again, no changes were observed between the two groups for the fibrosis-related gene mRNA levels even at 2 weeks after UUO (Figure 6C). Intriguingly, Western blot analyses demonstrated that fibronectin, α-SMA, and a large oligomeric ECM glycoprotein which also serves as a major component of the fibrotic KLM, Tenascin C (TNC) (Fu et al., 2017), were significantly increased in Lyz-met−/− mice fibrotic kidneys after IRI at 10 days or UUO at 7 days, compared with the Lyz-met+/+ controls (Figures 6D–6G). Consistently, Sirius red staining or Masson's trichrome staining further confirmed excessive collagen accumulation in Lyz-c-met−/− mice kidneys after IRI or UUO, compared with their littermate controls (Figures 6H and 6I). Immunofluorescence staining
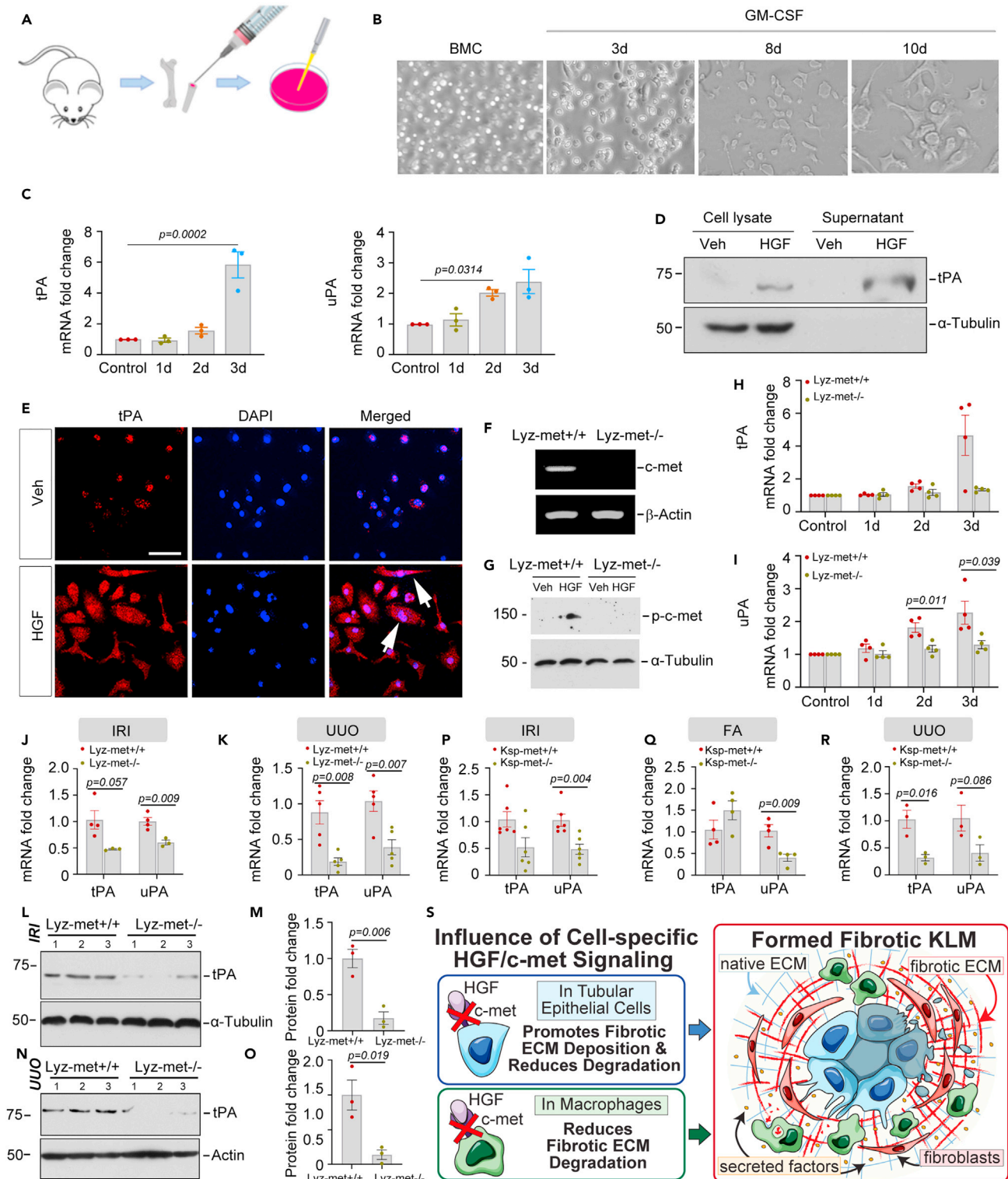
Figure 7. Macrophage loss of c-met repressed the capacity to degrade fibrotic ECM

(A) The strategy of bone marrow-derived macrophage (BMDMs) isolation and culture.

(B) Phase-contrast images of BMDM differentiation after stimulation with GM-CSF.

(C) qRT-PCR analysis of *tPA* and *uPA* mRNA in BMDMs after incubation with HGF recombinant protein (20 ng/mL) for 1, 2, or 3 days. n = 3.

(D) Western blot analyses demonstrating the induction of tPA in BMDMs after incubation with HGF recombinant protein (20 ng/mL).

Figure 7. Continued

(E) Immunostaining showing HGF-induced tPA expression in macrophages. Cells were co-stained with 4′,6-diamidino-2-phenylindole (DAPI) to visualize the nuclei. Scale bar, 25 μm.

(F) RT-PCR analysis showed *c-met* gene expression in cultured c-met+/+ and c-met−/− BMDMs *ex vivo*.

(G) Western blot analysis demonstrating reduced c-met phosphorylation after incubation with HGF recombinant protein in c-met−/− BMDMs.

(H and I) qRT-PCR analysis of *tPA* and *uPA* mRNA in cultured c-met+/+ and c-met−/− BMDMs after incubation with HGF recombinant protein (20 ng/mL) for 1, 2, or 3 days. n = 4.

(J and K) qPCR analysis revealing higher *tPA* and *uPA* mRNA abundance in Lyz-met+/+ than Lyz-met−/− kidneys after IRI and UUO. n = 3–5.

(L–O) Western blot analyses (L, N) and quantitative data (M, O) demonstrating tPA protein abundance in Lyz-met +/+ and Lyz-met−/− mice kidneys after IRI and UUO. Dots indicate individual animals within each group. n = 3.

(P–R) qRT-PCR analysis of *tPA*, and *uPA* mRNA in Ksp-met+/+ and Ksp-met−/− kidneys after IRI, FA, and UUO. n = 3–6.

(S) Schematic diagram of our model for fibrotic KLM formation. Data are represented as mean ± SEM. Statistical significance was assessed using a two-tailed Student's t-test or the Rank Sum Test if data failed in normality test or one-way ANOVA, followed by the Student-Newman-Keuls test.

revealed an increased level of fibronectin, type III collagen, and TNC in the Lyz-met−/− mice fibrotic kidneys, compared with the Lyz-c-met+/+ mice (Figures 6H and 6I, and S10). Of note, the quantitative assay determined that the ratio of collagen:non-collagen protein was 1.5∼2-fold higher in the Lyz-met−/− mice fibrotic kidneys after IRI or UUO, compared with Lyz-met+/+ controls (Figure 6J).

In comparison to tubular cells, macrophages possess a powerful capacity to secrete cytokines and chemokines into the interstitial spaces after kidney injury. To further assess the role of macrophage HGF/c-met in regulating fibrotic KLM formation, we examined pro-inflammatory cytokine expression in the fibrotic kidneys of Lyz-met+/+ and Lyz-met−/− mice. As shown in Figures 6K–6P, real-time qRT-PCR and Western blot analyses demonstrated that *MCP-1* mRNA and protein expression (respectively) were both significantly upregulated in Lyz-met−/− mice fibrotic kidneys after IRI or UUO, compared with their littermate controls. When compared with Lyz-met+/+ controls, immunohistochemical staining indicated that the loss of c-met in macrophages resulted in unusual secretion of RANTES and MCP-1 to the adjacent injured area, which can accelerate renal fibrosis (Figures 6Q and 6R). Surprisingly, 10 days after IRI, there was little difference between the numbers of F4/80+ macrophages in the fibrotic kidneys of Lyz-met+/+ and Lyz-met−/− mice, as demonstrated by flow cytometry assay (Figures 6S and 6T). This result suggested that loss of HGF/c-met in macrophages impairs their ability to control the secretion of detrimental factors that result in renal fibrosis progression. Together, these data indicate that loss of c-met in macrophages increases the risk of fibrotic KLM formation but does not affect the speed of ECM synthesis.

Macrophage loss of c-met repressed the capacity to degrade fibrotic ECM

A vital mechanism involved in fibrotic KLM formation is the dynamic balance between ECM synthesis and degradation. Secretion of ECM-degrading proteases plays a key role in regulating ECM turnover and degradation (Baricos et al., 1995; Yang et al., 2002). Since macrophage-derived c-met had little effect on ECM synthesis, we further investigated the function of macrophage HGF from another aspect – ECM degradation. To this end, we isolated monocytes from the bone marrow of mice and stimulated them with granulocyte-macrophage colony-stimulating factor (GM-CSF) to induce differentiation of bone marrow-derived macrophages (BMDMs; Figures 7A and 7B). BMDMs were incubated with HGF recombinant protein for 1, 2, or 3 days. Considering ECM-degrading proteases are key drivers of collagen degradation, we broadly profiled the expression of various proteases in the differentiated BMDMs. As shown in Figures 7C and S11A, HGF administration significantly increased the mRNA abundance of several ECM-degrading proteases including tissue plasminogen activator (tPA), urinary plasminogen activator (uPA), matrix metalloproteinases (MMPs; family members 1, 8, and 10), and tissue inhibitor of metalloproteinases-1 (TIMP-1). In addition, Western blot analyses demonstrated tPA protein was induced in the cells and supernatant after incubation with HGF recombinant protein *ex vivo* (Figure 7D). This result was confirmed by immunofluorescence staining (Figure 7E).

Since it was suggested that HGF promotes matrix-degrading protease production, we sought to further determine whether proteases are regulated by HGF/c-met signaling in macrophages. To address this issue, we isolated BMDMs from Lyz-met+/+ mice and Lyz-met−/− mice. RT-PCR analyses showed that the *c-met* gene was deleted in Lyz-met−/− BMDMs (Figure 7F). Consistently, after treatment with HGF recombinant protein, the induction of phosphorylated c-met was largely abolished in Lyz-met−/− BMDMs, compared with Lyz-met+/+ BMDM controls (Figure 7G). Meanwhile, Lyz-met−/− BMDMs exhibited diminished mRNA levels of *tPA* and *uPA* at 3 days after incubation with HGF, compared with Lyz-

met+/+ BMDM controls (Figures 7H and 7I). To validate this finding *ex vivo*, we further examined tPA and uPA levels in Lyz-met+/+ and Lyz-met−/− mice kidneys after IRI and UUO, respectively. As presented in Figures 7J and 7K, mRNA abundance of *tPA* and *uPA* were largely reduced in Lyz-met−/− mice, compared with Lyz-met+/+ controls. Additionally, tPA protein expression was markedly repressed in the fibrotic kidneys of Lyz-met−/− mice, compared with Lyz-met+/+ controls (Figures 7L–7O). Of note, the mRNA expression of *MMPs* did not change in the diseased kidneys between Lyz-met+/+ and Lyz-met−/− mice after IRI (Figure S11B). Most importantly, the gelatin degradation assay revealed that loss of c-met in macrophages largely inhibited the gelatinase activity both *in vitro* and *in vivo* which directly led to excessive ECM accumulation (Figures S11C–S11E). In addition, in renal tubules, loss of c-met also caused reduced mRNA levels of *tPA* and *uPA* in the fibrotic kidneys after IRI, FA injection, and UUO, compared with Ksp-met+/+ controls (Figures 7P–7R). Collectively, our data indicate that HGF/c-met signaling leads to the release of ECM-degrading proteases that influence fibrotic KLM formation.

DISCUSSION

As the name implies, the fibrotic KLM refers to special structures housing multiple cellular and non-cellular components that determine CKD progression. However, unlike the microenvironment in oncology, the concept of the fibrotic KLM has not been well documented in the kidney disease field thus far. In this study, by integrating data mining, mathematical model construction, and conditional knockout mouse models, we revisited how HGF signaling affects the construction of the fibrotic KLM as a key determinant in CKD progression. Our results suggest that (1) A fibrotic KLM is focal and segmental; (2) At the single-cell level, c-met, the receptor of HGF, is more enriched in the loop of Henle/distal convoluted tubules and collecting ducts in fibrotic kidneys than in macrophages; (3) Our mathematical model predicted that loss of c-met in tubular epithelial cells caused superior quick responses to simulated injures, compared with when c-met was ablated in macrophages; (4) Specific deletion of c-met in tubules influenced epithelial plasticity and accelerated synthesis of ECM after various CKD, but c-met deletion in macrophages had less of an impact; and (5) Loss of c-met in tubular cells or macrophages reduced tPA secretion resulting in impaired ECM degradation after CKD. We hypothesize that the heterogeneities of these different kidney cell types largely determine the features of the fibrotic KLM (Figure 7S).

Kidney cellular components are complex. They comprise at least 13 different epithelial cell types, surrounded by an even more extensive array of supporting vascular, stromal, and immune cells (Humphreys, 2018; Park et al., 2018). In all progressive CKD, aberrant activation and proliferation of fibroblasts are considered the major culprits in expanding matrix-producing cell populations that ultimately lead to renal fibrosis (Fu et al., 2017; LeBleu et al., 2013). The formation of a fibrotic KLM is a dynamic and converging process. For a long time, the primary focus in renal fibrosis has been how to halt excessive ECM accumulation (Duffield, 2014; Liu, 2011). Recent single-cell analysis clearly suggested that myofibroblasts arise from pericytes and fibroblasts. It revealed that the vast majority of ECM in human kidney fibrosis originates from mesenchymal cells, whereas de-differentiated proximal tubular cells play a minor role (Kuppe et al., 2021). However, as many major cell populations are involved in the fibrotic KLM, how to accurately weigh the direct or indirect contributions of tubular cells and macrophages during fibrotic KLM formation remains unclear.

A novelty of this study is that we characterized the fibrotic KLM from the perspective of tubular epithelial cells and macrophages. Through single-cell sequencing data mining, we revealed that the major cell populations in fibrotic kidneys are tubular epithelial cells and macrophages. Impressively, the proportion of c-met+ tubular cells is much greater than c-met+ macrophages in fibrotic kidneys (Figure 2). Although they are the largest cell population in the kidney, epithelial cells were previously considered victims or bystanders of CKD pathogenesis (Qi and Yang, 2018). Their involvement in the formation of the fibrotic KLM has been largely neglected. However, our mathematical model predicted that specifically depleting c-met receptor in tubular epithelial cells, but not in macrophages, would cause a more rapid response to simulated injuries (Figure 3). In fact, after kidney injury, loss of tubular c-met immediately led to increased cell apoptosis through intrinsic and extrinsic pathways during the acute phase (Zhou et al., 2013). The self-repair abilities of tubular cells were largely diminished due to the loss of c-met as well. This change resulted in the adaptive repair process becoming maladaptive along with disease progression (Ferenbach and Bonventre, 2015). Consequently, chronically injured Ksp-met−/− tubular cell-driven fibroblasts accumulate and transition to myofibroblasts by epithelial-mesenchymal communications (EMCs) rather than EMT, which was manifested by *de novo* α-SMA expression and augmented production of fibrillar collagen

(Figure 4). This EMC process was probably mediated by highly expressed Wnt and sonic hedgehog (data not shown) after loss of tubular c-met, as well as Snail 1, Twist, and Notch protein, as reported (Bielesz et al., 2010; Grande et al., 2015; Lovisa et al., 2015).

In the present study, we also revealed that loss of c-met in tubular epithelial cell decreased expression of E-cadherin (Figures S6, S7, and S8) and cells were activated to express vimentin in all three well-characterized CKD models: IRI, UUO, and FA injection (Figure 5). Although some reports consider vimentin as a regeneration marker for rat and human tubular cells (Kriz et al., 2011), it is indeed required for the plasticity of mesenchymal cells under normal physiological conditions and the migration of cancer cells undergoing EMT (Lu and Kang, 2019). Therefore, our data suggest that vimentin+ epithelial cells possess mesenchymal characteristics after CKD. Earlier studies suggested that injured tubular cells can transdifferentiate and convert to myofibroblasts via EMT. However, this controversial topic of EMT and the origin of myofibroblasts has long been debated (Kriz et al., 2011; Liu, 2010). Considering HGF is a potent effector of cell growth, movement, and differentiation, a tubular-specific loss of c-met mouse model would be an ideal tool to provide further evidence to clarify this issue. Unfortunately, in the current study, few epithelial cells could be observed crossing the tubular basement membrane even when using a 3D reconstruction technique in fibrotic kidneys of Ksp-met−/− mice or other genetic tools (Figure 5), as well as in human kidney biopsy specimens (Figure S7). Therefore, instead of complete EMT, the term "epithelial plasticity" or "partial EMT" is appropriate to describe this epithelial phenotypic change in the current study (Zhu et al., 2020). Epithelial plasticity refers to that, in a fibrotic kidney, a number of tubular cells possess the features of mesenchymal cells while others may transit back to the epithelial phenotype or remain in a dedifferentiated state (Huang and Susztak, 2016). Consistently, vimentin was expressed in epithelial cells in Ksp-met−/− mice fibrotic kidneys in all applied CKD models in this study, but not Ksp-met+/+ mice. The distributions of vimentin+ epithelial cells, especially, were completely heterogeneous in the fibrotic kidneys (Figure 5). Vimentin upregulation could increase epithelial cell stiffness, raise cell motility and migration, and increase epithelial plasticity due to E-cadherin loss and β1-integrin activation (Liu et al., 2015). We hypothesize that loss of c-met in tubular cells could be considered a second hit in epithelial cell phenotypic transition after CKD. On one hand, loss of c-met resulted in epithelial cells that lost their polarity while repairing themselves. On the other hand, injured tubular cells started becoming mesenchymal, which would make them an accomplice in ECM production during fibrotic KLM formation. Meanwhile, injured renal tubular epithelial cells become arrested at G2/M and adopt a profibrotic phenotype, which affects other epithelial cells and other neighboring cells, and accelerates renal fibrosis (Yang et al., 2010). Therefore, we conclude that tubular epithelial cells are active members of the fibrotic KLM after CKD.

Although c-met-deficient macrophages consistently caused accelerated kidney fibrosis, they had surprisingly little effect on ECM synthesis compared with tubular epithelial cells (Figure 6). Our mathematical model indicated a delayed response to simulated injury if c-met was deleted in macrophages (Figure 3). This may be because macrophage infiltration into the diseased kidney is not an early event. Based on the single-cell RNA-seq data, c-met+ macrophages were not a major population of the infiltrated cell pool in fibrotic kidneys (Figure 2). This may explain why macrophage-specific deletion of c-met did not induce fibrosis-related mRNA changes in multiple CKD models, compared with their littermate controls. Conversely, loss of c-met in macrophages or tubular epithelial cells consistently reduced the capacity to secrete tPA and uPA proteases (Figure 7). As a serine protease, tPA is a well-known plasminogen activator in the circulatory system that contains Kringle domains, similar to those in HGF. It plays a critical role in modulating the post-translational activation of HGF, as well as TGF-β (Hu et al., 2008). Together with its cousin serine protease uPA, they cleave plasminogen into plasmin during fibrinolysis. Plasmin is an important active enzyme that degrades insoluble fibrin fibers into small fragments which can be processed and removed by other proteases and the kidneys (Chapin and Hajjar, 2015). Meanwhile, tPA can also regulate the degradation of ECM through MMPs, which could be activated by plasmin (White et al., 2020). Decreased tPA level caused accumulation of fibrotic ECM and facilitated epithelial plasticity. In a fibrotic kidney, ECM is the backbone of the architectural changes of the local microenvironment. In this study, c-met-deficient macrophages caused the imbalance of ECM construction and destruction and directly accelerated fibrotic KLM formation (Figures 6 and 7, and S11). It should be emphasized that the majority of ECM components themselves can functionally serve as a "biologic glue" in establishing the fibrotic KLM by recruiting cellular components and sequestering secreted factors such as MCP-1, RANTES, TNF-α, and so on. Meanwhile, it allows the injured cells to rest on the fibrotic ECM, which drives the formation of the fibrotic KLM. As we already mentioned, kidney injury is heterogeneous. Based on our data, we hypothesize that the

density and sizes of the fibrotic KLM sites vary even in patients with similar severity of CKD, which may explain why patients have completely distinct courses while entering end-stage renal diseases.

In summary, by applying a multidisciplinary approach, we herein highlighted a reemerging concept – the fibrotic KLM in progressive CKD. We illustrated that HGF/c-met signaling in different cell types possesses distinct capacities to build the fibrotic KLM. Advances in our understanding of KLM open possibilities to decode the networks within KLM and to design effective therapeutic strategies to retard CKD in the clinic.

Limitations of the study

In this study, we elucidated the roles of epithelial cell- and macrophage-derived HGF/c-met signaling pathways during fibrotic KLM formation in parallel. The lateral connections between epithelial cells and macrophages have not been deeply explored. Therefore, more investigations into the communication among the various components are necessary to reveal the complexity of the fibrotic KLM. In addition, one technical weakness of this study is that, to minimize animal numbers in a single study, we did not includes sham controls for FA or IRI groups in both tubular- or macrophage-c-met conditional knockout mice, although it did not influence our final conclusions.

STAR★METHODS

Detailed methods are provided in the online version of this paper and include the following:

- KEY RESOURCES TABLE
- RESOURCE AVAILABILITY
  - Lead contact
  - Materials availability
  - Data and code availability
- EXPERIMENTAL MODEL AND SUBJECT DETAILS
- METHOD DETAILS
  - Public data mining
  - Mathematical model construction
  - Human kidney tissue sections
  - Automated analysis of fibrotic area in human kidney tissue
  - Mice and genotyping
  - Mouse models of CKD
  - Collagen/non-collagen assay
  - Gelatin degradation assay
  - Determination of serum creatinine
  - Histology and immunohistochemical staining
  - Immunofluorescence staining and confocal microscopy
  - Kidney macrophage suspensions and flow cytometry assay
  - Isolation and culture of bone marrow-derived macrophages (BMDMs)
  - Western blot analysis
  - Quantitative real-time reverse transcription PCR (qRT-PCR)
- QUANTIFICATION AND STATISTICAL ANALYSIS

SUPPLEMENTAL INFORMATION

Supplemental information can be found online at https://doi.org/10.1016/j.isci.2021.103112.

AUTHOR CONTRIBUTIONS

Conceptualization, H.F., Y.L., and D.Z.; methodology, H.F., S.L., X.-J.T., and D.Z; investigation, H.F., Y.G., S.L., Y.W., Y.Q., R.Z., Y.Y., B.P., Y.Z., X.-J.T., and D.Z.; writing – original draft, H.F., Y.G., X.-J.T., and D.Z.; writing – review& editing, H.F., Y.G., B.S., B.C., H.G., K.D., Y.W., X.-J.T., Y.L., and D.Z.; funding acquisition, X.-J.T., Y.L., and D.Z.; resources and supervision, Y.L. and D.Z.

DECLARATION OF INTERESTS

The authors declare no conflict of interest.

INCLUSION AND DIVERSITY

We worked to ensure gender balance in the recruitment of human subjects. We worked to ensure sex balance in the selection of non-human subjects.

REFERENCES

Anders, H.J., and Ryu, M. (2011). Renal microenvironments and macrophage phenotypes determine progression or resolution of renal inflammation and fibrosis. Kidney Int. 80, 915–925.

Baricos, W.H., Cortez, S.L., el-Dahr, S.S., and Schnaper, H.W. (1995). ECM degradation by cultured human mesangial cells is mediated by a PA/plasmin/MMP-2 cascade. Kidney Int. 47, 1039–1047.

Bielesz, B., Sirin, Y., Si, H., Niranjan, T., Gruenwald, A., Ahn, S., Kato, H., Pullman, J., Gessler, M., Haase, V.H., et al. (2010). Epithelial notch signaling regulates interstitial fibrosis development in the kidneys of mice and humans. J. Clin. Invest 120, 4040–4054.

Chang-Panesso, M., and Humphreys, B.D. (2017). Cellular plasticity in kidney injury and repair. Nat. Rev. Nephrol. 13, 39–46.

Chapin, J.C., and Hajjar, K.A. (2015). Fibrinolysis and the control of blood coagulation. Blood Rev. 29, 17–24.

Conway, B.R., O'Sullivan, E.D., Cairns, C., O'Sullivan, J., Simpson, D.J., Salzano, A., Connor, K., Ding, P., Humphries, D., Stewart, K., et al. (2020). Kidney single-cell atlas reveals myeloid heterogeneity in progression and regression of kidney disease. J. Am. Soc. Nephrol. 31, 2833–2854.

Duffield, J.S. (2014). Cellular and molecular mechanisms in kidney fibrosis. J. Clin. Invest 124, 2299–2306.

Feng, Y., Ren, J., Gui, Y., Wei, W., Shu, B., Lu, Q., Xue, X., Sun, X., He, W., Yang, J., et al. (2018). Wnt/beta-catenin-promoted macrophage alternative activation contributes to kidney fibrosis. J. Am. Soc. Nephrol. 29, 182–193.

Ferenbach, D.A., and Bonventre, J.V. (2015). Mechanisms of maladaptive repair after AKI leading to accelerated kidney ageing and CKD. Nat. Rev. Nephrol. 11, 264–276.

Fu, H., Tian, Y., Zhou, L., Zhou, D., Tan, R.J., Stolz, D.B., and Liu, Y. (2017). Tenascin-C Is a major component of the fibrogenic niche in kidney fibrosis. J. Am. Soc. Nephrol. 28, 785–801.

Grande, M.T., Sanchez-Laorden, B., Lopez-Blau, C., De Frutos, C.A., Boutet, A., Arevalo, M., Rowe, R.G., Weiss, S.J., Lopez-Novoa, J.M., and Nieto, M.A. (2015). Snail1-induced partial epithelial-to-mesenchymal transition drives renal fibrosis in mice and can be targeted to reverse established disease. Nat. Med. 21, 989–997.

Hao, Y., Hao, S., Andersen-Nissen, E., Mauck, W.M., 3rd, Zheng, S., Butler, A., Lee, M.J., Wilk, A.J., Darby, C., Zager, M., et al. (2021). Integrated analysis of multimodal single-cell data. Cell 184, 3573–3587.

Hu, K., Mars, W.M., and Liu, Y. (2008). Novel actions of tissue-type plasminogen activator in chronic kidney disease. Front Biosci. 13, 5174–5186.

Huang, S., and Susztak, K. (2016). Epithelial plasticity versus EMT in kidney fibrosis. Trends Mol. Med. 22, 4–6.

Humphreys, B.D. (2018). Mapping kidney cellular complexity. Science 360, 709–710.

Kramann, R., Fleig, S.V., Schneider, R.K., Fabian, S.L., DiRocco, D.P., Maarouf, O., Wongboonsin, J., Ikeda, Y., Heckl, D., Chang, S.L., et al. (2015). Pharmacological GLI2 inhibition prevents myofibroblast cell-cycle progression and reduces kidney fibrosis. J. Clin. Invest 125, 2935–2951.

Kriz, W., Kaissling, B., and Le Hir, M. (2011). Epithelial-mesenchymal transition (EMT) in kidney fibrosis: fact or fantasy? J. Clin. Invest 121, 468–474.

Kuppe, C., Ibrahim, M.M., Kranz, J., Zhang, X., Ziegler, S., Perales-Paton, J., Jansen, J., Reimer, K.C., Smith, J.R., Dobie, R., et al. (2021). Decoding myofibroblast origins in human kidney fibrosis. Nature 589, 281–286.

LeBleu, V.S., Taduri, G., O'Connell, J., Teng, Y., Cooke, V.G., Woda, C., Sugimoto, H., and Kalluri, R. (2013). Origin and function of myofibroblasts in kidney fibrosis. Nat. Med. 19, 1047–1053.

Liu, C.Y., Lin, H.H., Tang, M.J., and Wang, Y.K. (2015). Vimentin contributes to epithelial-mesenchymal transition cancer cell mechanics by mediating cytoskeletal organization and focal adhesion maturation. Oncotarget 6, 15966–15983.

Liu, Y. (2002). Hepatocyte growth factor and the kidney. Curr. Opin. Nephrol. Hypertens. 11, 23–30.

Liu, Y. (2010). New insights into epithelial-mesenchymal transition in kidney fibrosis. J. Am. Soc. Nephrol. 21, 212–222.

Liu, Y. (2011). Cellular and molecular mechanisms of renal fibrosis. Nat. Rev. Nephrol. 7, 684–696.

Lovisa, S., LeBleu, V.S., Tampe, B., Sugimoto, H., Vadnagara, K., Carstens, J.L., Wu, C.C., Hagos, Y., Burckhardt, B.C., Pentcheva-Hoang, T., et al. (2015). Epithelial-to-mesenchymal transition induces cell cycle arrest and parenchymal damage in renal fibrosis. Nat. Med. 21, 998–1009.

Lovisa, S., Zeisberg, M., and Kalluri, R. (2016). Partial epithelial-to-mesenchymal transition and other new mechanisms of kidney fibrosis. Trends Endocrinol. Metab. 27, 681–695.

Lu, J., Cao, Q., Zheng, D., Sun, Y., Wang, C., Yu, X., Wang, Y., Lee, V.W., Zheng, G., Tan, T.K., et al. (2013). Discrete functions of M2a and M2c macrophage subsets determine their relative efficacy in treating chronic kidney disease. Kidney Int. 84, 745–755.

Lu, W., and Kang, Y. (2019). Epithelial-mesenchymal plasticity in cancer progression and metastasis. Dev. Cell 49, 361–374.

Maarouf, O.H., Aravamudhan, A., Rangarajan, D., Kusaba, T., Zhang, V., Welborn, J., Gauvin, D., Hou, X., Kramann, R., and Humphreys, B.D. (2016). Paracrine Wnt1 drives interstitial fibrosis

without inflammation by tubulointerstitial cross-talk. J. Am. Soc. Nephrol. 27, 781–790.

Matsumoto, K., and Nakamura, T. (2001). Hepatocyte growth factor: renotropic role and potential therapeutics for renal diseases. Kidney Int. 59, 2023–2038.

McInnes, L., Healy, J., and Melville, J. (2018). UMAP: Uniform Manifold Approximation and Projection for Dimension Reduction, arXiv:1802.03426.

Na, Y.R., Gu, G.J., Jung, D., Kim, Y.W., Na, J., Woo, J.S., Cho, J.Y., Youn, H., and Seok, S.H. (2016). GM-CSF induces inflammatory macrophages by regulating glycolysis and lipid metabolism. J. Immunol. 197, 4101–4109.

Nieto, M.A. (2013). Epithelial plasticity: a common theme in embryonic and cancer cells. Science 342, 1234850.

Noriega-Guerra, H., and Freitas, V.M. (2018). Extracellular matrix influencing HGF/c-MET signaling pathway: impact on cancer progression. Int. J. Mol. Sci. 19, 3300.

Park, J., Shrestha, R., Qiu, C., Kondo, A., Huang, S., Werth, M., Li, M., Barasch, J., and Susztak, K. (2018). Single-cell transcriptomics of the mouse kidney reveals potential cellular targets of kidney disease. Science 360, 758–763.

Perry, H.M., Gorldt, N., Sung, S.J., Huang, L., Rudnicka, K.P., Encarnacion, I.M., Bajwa, A., Tanaka, S., Poudel, N., Yao, J., et al. (2019). Perivascular CD73(+) cells attenuate inflammation and interstitial fibrosis in the kidney microenvironment. Am. J. Physiol. Ren. Physiol 317, F658–F669.

Prunotto, M., and Moll, S. (2011). The emerging concept of a fibrotic microenvironment in CKD. Kidney Int. 79, 135.

Qi, R., and Yang, C. (2018). Renal tubular epithelial cells: the neglected mediator of tubulointerstitial fibrosis after injury. Cell Death Dis 9, 1126.

Ramani, K., Jawale, C.V., Verma, A.H., Coleman, B.M., Kolls, J.K., and Biswas, P.S. (2018). Unexpected kidney-restricted role for IL-17 receptor signaling in defense against systemic Candida albicans infection. JCI Insight 3, e98241.

Ren, J., Zhang, J., Rudemiller, N.P., Griffiths, R., Wen, Y., Lu, X., Privratsky, J.R., Gunn, M.D., and

Crowley, S.D. (2019). Twist1 in infiltrating macrophages attenuates kidney fibrosis via matrix metallopeptidase 13-mediated matrix degradation. J. Am. Soc. Nephrol. 30, 1674–1685.

Ruiz-Ortega, M., Rayego-Mateos, S., Lamas, S., Ortiz, A., and Rodrigues-Diez, R.R. (2020). Targeting the progression of chronic kidney disease. Nat. Rev. Nephrol. 16, 269–288.

Saitoh, M. (2018). Involvement of partial EMT in cancer progression. J. Biochem. 164, 257–264.

Shao, X., Somlo, S., and Igarashi, P. (2002). Epithelial-specific Cre/lox recombination in the developing kidney and genitourinary tract. J. Am. Soc. Nephrol. 13, 1837–1846.

Sheng, L., and Zhuang, S. (2020). New insights into the role and mechanism of partial epithelial-mesenchymal transition in kidney fibrosis. Front Physiol. 11, 569322.

Stuart, T., Butler, A., Hoffman, P., Hafemeister, C., Papalexi, E., Mauck, W.M., 3rd, Hao, Y., Stoeckius, M., Smibert, P., and Satija, R. (2019). Comprehensive integration of single-cell data. Cell 177, 1888–1902.

Tian, X.J., Zhou, D., Fu, H., Zhang, R., Wang, X., Huang, S., Liu, Y., and Xing, J. (2020). Sequential Wnt agonist then antagonist treatment accelerates tissue repair and minimizes fibrosis. iScience 23, 101047.

Wen, Y., Lu, X., Ren, J., Privratsky, J.R., Yang, B., Rudemiller, N.P., Zhang, J., Griffiths, R., Jain, M.K., Nedospasov, S.A., et al. (2019). KLF4 in macrophages attenuates TNFalpha-mediated kidney injury and fibrosis. J. Am. Soc. Nephrol. 30, 1925–1938.

White, S., Lin, L., and Hu, K. (2020). NF-kappaB and tPA signaling in kidney and other diseases. Cells 9, 1348.

Wu, H., Kirita, Y., Donnelly, E.L., and Humphreys, B.D. (2019). Advantages of single-nucleus over single-cell RNA sequencing of adult kidney: rare cell types and novel cell states revealed in fibrosis. J. Am. Soc. Nephrol. 30, 23–32.

Wu, H., Lai, C.F., Chang-Panesso, M., and Humphreys, B.D. (2020). Proximal tubule translational profiling during kidney fibrosis reveals proinflammatory and long noncoding RNA expression patterns with sexual dimorphism. J. Am. Soc. Nephrol. 31, 23–38.

Yang, J., Dai, C., and Liu, Y. (2003). Hepatocyte growth factor suppresses renal interstitial myofibroblast activation and intercepts Smad signal transduction. Am. J. Pathol. 163, 621–632.

Yang, J., Dai, C., and Liu, Y. (2005). A novel mechanism by which hepatocyte growth factor blocks tubular epithelial to mesenchymal transition. J. Am. Soc. Nephrol. 16, 68–78.

Yang, J., Shultz, R.W., Mars, W.M., Wegner, R.E., Li, Y., Dai, C., Nejak, K., and Liu, Y. (2002). Disruption of tissue-type plasminogen activator gene in mice reduces renal interstitial fibrosis in obstructive nephropathy. J. Clin. Invest 110, 1525–1538.

Yang, L., Besschetnova, T.Y., Brooks, C.R., Shah, J.V., and Bonventre, J.V. (2010). Epithelial cell cycle arrest in G2/M mediates kidney fibrosis after injury. Nat. Med. 16, 535–543.

Yu, M.A., Shin, K.S., Kim, J.H., Kim, Y.I., Chung, S.S., Park, S.H., Kim, Y.L., and Kang, D.H. (2009). HGF and BMP-7 ameliorate high glucose-induced epithelial-to-mesenchymal transition of peritoneal mesothelium. J. Am. Soc. Nephrol. 20, 567–581.

Zhou, D., Fu, H., Xiao, L., Mo, H., Zhuo, H., Tian, X., Lin, L., Xing, J., and Liu, Y. (2018). Fibroblast-specific beta-catenin signaling dictates the outcome of AKI. J. Am. Soc. Nephrol. 29, 1257–1271.

Zhou, D., Fu, H., Zhang, L., Zhang, K., Min, Y., Xiao, L., Lin, L., Bastacky, S.I., and Liu, Y. (2017). Tubule-derived wnts are required for fibroblast activation and kidney fibrosis. J. Am. Soc. Nephrol. 28, 2322–2336.

Zhou, D., Li, Y., Zhou, L., Tan, R.J., Xiao, L., Liang, M., Hou, F.F., and Liu, Y. (2014). Sonic hedgehog is a novel tubule-derived growth factor for interstitial fibroblasts after kidney injury. J. Am. Soc. Nephrol. 25, 2187–2200.

Zhou, D., Tan, R.J., Lin, L., Zhou, L., and Liu, Y. (2013). Activation of hepatocyte growth factor receptor, c-met, in renal tubules is required for renoprotection after acute kidney injury. Kidney Int. 84, 509–520.

Zhu, H., Liao, J., Zhou, X., Hong, X., Song, D., Hou, F.F., Liu, Y., and Fu, H. (2020). Tenascin-C promotes acute kidney injury to chronic kidney disease progression by impairing tubular integrity via alphavbeta6 integrin signaling. Kidney Int. 97, 1017–1031.

STAR★METHODS

KEY RESOURCES TABLE

REAGENT or RESOURCE	SOURCE	IDENTIFIER
Antibodies		
anti-α-SMA	Abcam	Cat# ab5694; RRID:AB_2223021
anti-CD68	Abcam	Cat# ab213363; RRID:AB_2801637
anti-CD14	Abcam	Cat# ab133335; RRID:AB_2889158
anti-TNC	Abcam	Cat# ab6346; RRID:AB_305439
anti-F4/80	Bio-Rad	Cat# MCA497GA; RRID:AB_323806
anti-E-cadherin	BD Biosciences	Cat# 610181; RRID:AB_397580
anti-E-cadherin	Cell Signaling Technology	Cat# 3195; RRID:AB_2291471
anti-Vimentin	Cell Signaling Technology	Cat# 5741; RRID:AB_10695459
anti-p-c-met	Cell Signaling Technology	Cat# 3126; RRID:AB_331713
anti-GAPDH	Cell Signaling Technology	Cat# 5174; RRID:AB_10622025
anti-RANTES	Fitzgerald Industries International	Cat# 10R-R121A; RRID:AB_10809986
anti-tPA	Oxford Biomedical Research	Cat# PT34; RRID:AB_10818863
anti-uPA	Proteintech	Cat 17968-1-AP; RRID:AB_2165202
anti-AQP1	Proteintech	Cat# 20333-1-AP; RRID:AB_10666159
anti-met	Santa Cruz Biotechnology	Cat# sc-8057; RRID:AB_673755
anti-AQP3	Sigma Aldrich	SAB5200111
anti-NCC	Sigma Aldrich	Cat# AB3553; RRID:AB_571116
anti-Fibronectin	Sigma Aldrich	Cat# F3648; RRID:AB_476976
anti-α-SMA	Sigma Aldrich	Cat# A2547; RRID:AB_476701
anti-Laminin	Sigma Aldrich	Cat# L8271; RRID:AB_477162
anti-α-Tubulin	Sigma Aldrich	Cat# T9026; RRID:AB_477593
anti-Collagen Type III	Sigma Aldrich-Millipore	Cat# AB747; RRID:AB_11211895
anti-Actin	Sigma Aldrich-Millipore	Cat# MAB1501; RRID:AB_2223041
anti-CD11b (eBioscience™)	ThermoFisher Scientific	Cat# 14-0112-82; RRID:AB_467108
anti-F4/80 (eBioscience™)	ThermoFisher Scientific	Cat# 14-4801-82; RRID:AB_467558
anti-MCP-1	ThermoFisher Scientific	Cat# PA5-34505; RRID:AB_2551857
Cy3-AffiniPure Donkey Anti-Mouse IgG	Jackson ImmunoResearch	Cat# 715-165-150; RRID:AB_2340813
Cy3-AffiniPure Donkey Anti-Rabbit IgG	Jackson ImmunoResearch	Cat# 711-165-152; RRID:AB_2307443
Alexa Fluor® 488-AffiniPure Donkey Anti-Rabbit IgG	Jackson ImmunoResearch	Cat# 711-545-152; RRID:AB_2313584
Biotin-SP-AffiniPure Donkey Anti-Mouse IgG	Jackson ImmunoResearch	Cat# 715-065-150; RRID:AB_2307438
Biotin-SP-AffiniPure Donkey Anti-Rabbit IgG	Jackson ImmunoResearch	Cat# 711-065-152; RRID:AB_2340593
Biotin-SP-AffiniPure Donkey Anti-Rat IgG	Jackson ImmunoResearch	Cat# 712-065-153; RRID:AB_2315779
anti-Collagen I	Cell Signaling Technology	Cat#72026
Critical commercial assays		
Gelatin Degradation Assay Kit	Abcam	ab234057
QuantiChrom Creatinine Assay Kit	BioAssay Systems	DICT-500
Sirius Red/Fast Green Collagen Staining Kit	Chondrex, Inc.	#9046
Trichrome Stain Kit	Sigma Aldrich	HT15-1KT

Continued

REAGENT or RESOURCE	SOURCE	IDENTIFIER
Experimental models: organisms/strains		
C-met floxed mouse (FVB;129P2-Mettm1Sst/J)	National Cancer Institute	Provided by Dr. Snorri S. Thorgeirsson
Ksp-Cre mouse (B6.Cg-Tg(Cdh16-cre)91Igr/J)	University of Minnesota Medical School	Provided by Dr. Peter Igarashi
Lyz2-Cre (B6.129P2-Lyz2tm1(cre)Ifo/J)	University of Pittsburgh School of Medicine	Provided by Dr. Wendy M. Mars
Ai9 mice (B6.Cg-Gt(ROSA)26Sortm9 (CAG-tdTomato)Hze/J)	The Jackson Laboratory	Stock No. 007909
Oligonucleotides		
Primers, see Table S2	This paper	N/A
Software and algorithms		
The R-project for Statistical Computing	R Foundation (version 4.0.3)	https://www.r-project.org/
R/Bioconductor package	Seurat 4.0.4	https://satijalab.org/seurat/
The script for quantification of the immunohistochemical staining images	This paper (Material S1)	N/A
Matlab (R2017a)	MathWorks	https://www.mathworks.com/
OSCILL8	Oscill8	http://oscill8.sourceforge.net/
Prism9	GraphPad Software	http://www.graphpad.com/
Image Pro plus 6.0	Media Cybernetics	https://www.mediacy.com/
FlowJo	Tree Star Inc.	http://www.treestar.com/

RESOURCE AVAILABILITY

Lead contact

Further information and requests for data should be directed to and will be fulfilled by the lead contact, Dong Zhou (dzhou@uchc.edu).

Materials availability

This study did not generate new unique reagents.

Data and code availability

Data: All data produced or analyzed for this study are included in the published article and its supplementary files or are available from the corresponding author upon reasonable request.

Code: The script for quantification of the immunohistochemical staining images can be found in Material S1. R/Bioconductor package (Seurat 4.0.4) for public data mining was obtained from the Satija lab.

Other items: All the equations and parameters of the mathematical models can be found in the Method Details.

EXPERIMENTAL MODEL AND SUBJECT DETAILS

Tubular- or macrophages- *c-met* conditional knockout mice were generated by mating *c-met* floxed mice (FVB;129P2-Mettm1Sst/J, provided by Dr. Snorri S. Thorgeirsson) with the transgenic mice that expressed Cre recombinase under the control of kidney-specific-cadherin (Ksp) promoter (B6.Cg-Tg(Cdh16-cre) 91Igr/J, provided by Dr. Peter Igarashi) or myeloid-specific promoter (B6.129P2-Lyz2tm1(cre)Ifo/J, provided by Dr. Wendy M. Mars), respectively. Ai9 mice (B6.Cg-Gt(ROSA)26Sortm9(CAG-tdTomato)Hze/J) expressing robust tdTomato fluorescence were purchased from the Jackson Laboratory (Stock No. 007909). Tubular tdTomato−/− mice were generated by mating Ai9 mice with Ksp-Cadherin promoter-driven Cre mice. 8-10 weeks old male and female mice were used for CKD animal models construction. All procedures were performed in accordance with the National Institutes of Health Guide for Laboratory Animals and were approved by the Institutional Animal Care and Use Committee at the University of Pittsburgh, School of Medicine (Protocol number: 16048123), and the University of Connecticut, School of Medicine (Protocol number: AP-200105-0923).

METHOD DETAILS

Public data mining

Two published studies were explored in this study (Conway et al., 2020; Wu et al., 2020). RNA-seq transcriptome profile GSE125015 was downloaded from GEO database and the gene fragments per kilobase of transcript per million mapped reads (FPKM) values were log2 scaled and normalized. Study GSE140023 was accessed via GEO database and the single-cell data were processed by R package Seurat (Hao et al., 2021; Stuart et al., 2019). Based on the gene-by-cell expression matrix, dimension reduction was performed by Uniform Manifold Approximation and Projection (UMAP) algorithm (McInnes et al., 2018). All the cells were eventually visualized in 2D scale, where UMAP_1 represents the first reduced dimension and UMAP_2 stands for the second dimension. Each dot in the UMAP figure indicates one cell and the cells were colored by library or by marker expression level.

Mathematical model construction

We built a mathematical model to explore the cell-cell communications between the tubular epithelial cells and macrophages during the formation of the fibrotic KLM. Following our previous work (Tian et al., 2020), we considered three groups in the tubular module, including normal tubular epithelial cells (E), injured tubular cells (I), and tubular cells undergoing phenotypic changes (P). In this module, some tubular cells will be injured due to the external stimulus. These injured tubular cells can be repaired to normal condition or die. Some of the tubular cells could be triggered into a phenotypic transition, which will secrete various cytokines, and promote ECM production and the formation of the fibrotic microenvironment (Grande et al., 2015). Meanwhile, injured tubular cells promote macrophage activation (Anders and Ryu, 2011). The activated macrophages promote the degradation of the ECM by secreting matrix metalloproteinases (MMPs) (Lu et al., 2013). The formed microenvironment in turn promotes the tubular epithelial cells to possess mesenchymal characteristics and macrophage activation. In this work, we focus on the roles of tubular epithelial cells and macrophages and the HGF/c-met signaling pathway in KLM formation. In the model, the HGF/c-met signaling in tubular epithelial cells inhibits the phenotypic transition of tubular epithelial cells and excessive ECM synthesis. In comparison, macrophage HGF/c-met signaling promotes the degradation of ECM. By considering all of these interactions and regulations, we developed the following coarse-grained ordinary differential equations (ODE) model:

$$\frac{dI}{dt} = k_{repair} \cdot I \cdot P - k_d \cdot I$$

$$\frac{dE}{dt} = k_{repair} \cdot I \cdot P - \left(k_{ep1} \cdot \frac{M^2}{M^2 + J_{ep1}^2} \cdot E + k_{ep2} \cdot \frac{ECM^{n1}}{ECM^n + J_{ep2}^{n1}} \cdot E \right) \cdot \frac{1}{HGF_P + 1} + k_{pe} \cdot P + k_{reg} \cdot E * O$$

$$\frac{dP}{dt} = \left(k_{ep1} \cdot \frac{M^2}{M^2 + J_{ep1}^2} \cdot E + k_{ep2} \cdot \frac{ECM^{n1}}{ECM^{n1} + J_{ep2}^{n1}} \cdot E \right) \cdot \frac{1}{HGF_P + 1} - k_{pe} \cdot P$$

$$\frac{dECM}{dt} = k_{ECM} \cdot P - ECM \cdot \left(d_{ECM0} + d_{ECM1} \cdot \frac{M^2}{M^2 + J_{ECM}^2} \cdot HGF_M \right)$$

$$\frac{dM}{dt} = k_{m0} + k_{m1} \cdot \frac{I^2}{I^{n1} + J_{m1}^{n1}} + k_{m2} \cdot \frac{ECM^{n2}}{ECM^{n2} + J_{m2}^{n2}} - kd_M \cdot M$$

where I, E, P, ECM, M are the relative levels of the injured tubular cells, normal tubular cells, the tubular cells in the partial epithelial to mesenchymal transition (EMT) state, ECM, and macrophage. $O = 100 - E - P - I$. While we did not find quantitative data to faithfully estimate the parameter values, we found that the model outcome is largely insensitive to the exact forms of the equation's terms and parameter values with systematic numerical tests. The model needs some degree of nonlinearity in some of the equation terms (Hill-type production functions), which is valid in most of the biological regulations, especially the cell transition as partial epithelial to mesenchymal transition and macrophage activation here. Here, for simplicity, we used all the Hill coefficients as 2 to allow sufficient overall nonlinearity. However, the conclusion does not depend on the exact values of the parameters as demonstrated by the parameter sensitivity analysis (Figure S2). The parameter values, unless otherwise mentioned, are $HGF_P = 2$, $HGF_M = 2$, $k_{repair} = .1$, $k_d = 0.1$, $k_{reg} = 0.01$, $k_{ep1} = 2$, $J_{ep1} = 5$, $k_{ep2} = 0.5$, $J_{ep2} = 10$, $n1 = 2$, $k_{pe} = 1$, $k_{m0} = 0.01$, $k_{m1} = 0.4$, $J_{m1} = 2$, $k_{m2} = 2$, $J_{m2} = 1$, $kd_M = 1$, $n2 = 2$, $k_{ECM} = .88$, $d_{ECM0} = 1$, $J_{ECM} = 1$, $d_{ECM1} = 0.5$. The levels of HGF in the tubular epithelial cells and macrophages were controlled by parameters HGF_P and HGF_M for simulating the knockdown experiments. For the parameter sensitivity analysis, each parameter was increased or decreased by 15% to study the dependence of the fibrosis thresholds in the WT, E-HGF

c-met−/−, and M-HGF c-met−/− on the parameter variation. Numerical bifurcation analysis was performed with OSCILL8 (http://oscill8.sourceforge.net/), while the time-course simulation was performed with MATLAB (R2017a) function ode23s. Repair time score was defined as the summation of the time for the system to repair and regenerate until the damage (I) below 0.1 unit for a series of injuries from 1 to 30 units. The fibrosis score was defined as the summation of the maximum level of ECM during the regeneration process for a series of injuries from 1 to 30 units.

Human kidney tissue sections

Human kidney biopsy specimen sections and non-tumor kidney tissue sections were obtained from the pathology archive at the University of Pittsburgh Medical Center. Non-tumor kidney tissue samples from the patients who had renal cell carcinoma and underwent nephrectomy were used as normal controls. All patients included in the presented study have signed the informed consent forms before they underwent kidney biopsy or nephrectomy. All procedures performed in the present study involving human kidney sections were following ethical standards and approved by the Institutional Review Board at the University of Pittsburgh, School of Medicine.

Automated analysis of fibrotic area in human kidney tissue

Ten random fields were selected in the cortical area for each kidney section in the MTS and Sirius red stained slides. The percentage of the interstitial fibrotic area was analyzed with a custom script in Image Pro plus 6.0 (Material 1). An average percentage of the kidney fibrotic area for each section was calculated. In this study, the blue channel was chosen because it had the best separation, as we previously described (Zhou et al., 2018). In brief, by using the "Threshold" tool, the threshold was set for (0, 80) to get the (red) areas where each marker was expressed at a high level. The threshold values were chosen manually until each stained marker was highlighted in red but the same thresholds were used for all images for each marker. The script in Supplemental Material S1 was used for the automated analysis of the immunohistochemistry staining images.

Mice and genotyping

C-met floxed mice (FVB;129P2-Met[tm1Sst]/J) were created by homologous recombination using a c-met gene fragment with loxP sites flanking exon 16, as described previously (Zhou et al., 2013), and were kindly provided by Dr. Snorri S. Thorgeirsson (National Cancer Institute, NIH, Bethesda, MD, USA). Transgenic mice that expressed Cre recombinase under the control of kidney-specific-cadherin promoter (B6.Cg-Tg(Cdh16-cre)91Igr/J) were generated as reported elsewhere (Shao et al., 2002). Transgenic mice that expressed Cre recombinase under the control of myeloid-specific promoter (B6.129P2-Lyz2[tm1(cre)Ifo]/J) were kindly provided by Dr. Wendy M. Mars (University of Pittsburgh, Pittsburgh, PA, USA). Conditional knockout mice Ksp-met−/− and Lyz-met−/− were generated by mating c-met floxed mice with Ksp-Cre transgenic mice and Lyz-Cre transgenic mice, respectively. The same gender littermates with Ksp-met+/+ and Lyz-met+/+ were considered as littermate controls, respectively. A routine PCR protocol was used for genotyping of tail DNA samples with the following primer pairs: Cre transgene, sense: 5'-AGGTGTAGAGAAGGCACTTAGC-3'; antisense: 5'-CTAATCGCCATCTTCCAGCAGG-3', which generated a 411 bp fragment; and c-met genotyping, 5'-TTAGGCAATGAGGTGTCCCAC-3' and 5'-CCAGGTGGCTTCAAATTCTAA-3', which yielded a 380 bp fragment for the floxed alleles. In a separate study, Ai9 mice (B6.Cg-Gt(ROSA)26Sor[tm9(CAG-tdTomato)Hze]/J) expressing robust tdTomato fluorescence were purchased from the Jackson Laboratory (#007909, Bar Harbor, Maine). Conditional knockout Ksp-tdTomato−/− mice were generated by mating Ai9 mice with Ksp-Cre tool mice. All animals were born normally at the expected Mendelian frequencies. At baseline, they were normal in size and did not display any gross physical or behavioral abnormalities. Animal experiments were approved by the Institutional Animal Care and Use Committee at the University of Pittsburgh, School of Medicine (Protocol number: 16048123), and the University of Connecticut, School of Medicine (Protocol number: AP-200105-0923).

Mouse models of CKD

CKD in mice was induced by three methods: folic acid (FA) injection, unilateral ureteral obstruction (UUO), and ischemic reperfusion injury (IRI). The FA model involved a single intraperitoneal injection of folic acid (Sigma, St. Louis, MO) dissolved in 150 mM sodium bicarbonate (vehicle) at 250 mg/kg body weight, sacrifice 60 days after injection, and kidney sample collection for analyses. UUO and IRI mice models were established using routine methods as previously described (Fu et al., 2017; Zhou et al., 2017).

Collagen/non-collagen assay

Paraffin-embedded mouse kidney sections (20 μm thickness) were prepared by a routine procedure (Zhou et al., 2017). The collagenous/non-collagenous protein ratio was measured using the Sirius red/fast green collagen staining kit, according to the protocols specified by the manufacturer (#9046, Chondrex, WA, USA). The OD values of the extracted dyes at 540 nm and 605 nm wavelength were used to calculate fibrotic kidneys' collagenous and non-collagenous protein content (and ratio).

Gelatin degradation assay

According to the manufacturer's protocol, the gelatinase activity was measured using a Gelatin Degradation Assay Kit (ab234057, Abcam Inc., Cambridge, MA, USA). In brief, 5-10 mg of frozen kidney tissue or 1-2 x10^6 cells were homogenized with lysis buffer and centrifuged to get supernatant. The amount of protein in the lysate was measured using the BCA protein assay kit (K813-500, BioVision Inc, San Francisco, CA, USA). 50 μL of lysate was added into desired wells in a white 96-well plate with 50 μL Gelatinase substrate mix per well. Wells were mixed and fluorescence was measured at Ex/Em 490/520 nm in kinetic mode at 37°C for 1 hour. FITC standard and positive control were included. The relative fluorescence unit (RFU)/min of each sample was used to calculate the gelatinase activity.

Determination of serum creatinine

Serum was collected from mice 60 days after FA injection or 10 days after IRI. Serum creatinine level was determined using a QuantiChrom creatinine assay kit, according to the protocols specified by the manufacturer (BioAssay Systems, USA). The level of serum creatinine was expressed as milligrams per 100 mL (dL).

Histology and immunohistochemical staining

Paraffin-embedded human kidney biopsy sections (2.5-μm thickness) and mouse kidney sections (3 μm thickness) were prepared by a routine procedure. The sections were stained with Masson's trichrome reagent and Sirius red (separately) by standard protocol (Zhou et al., 2017). Immunohistochemical staining was performed according to the established protocol as described previously. (Zhou et al., 2017) Antibodies used were: anti-α-SMA (ab5694), anti-CD68 (ab213363), anti-CD14 (ab133335, Abcam Inc., Cambridge, MA), anti-collagen I (#72026), anti-vimentin (#5741; Cell Signaling Technology, Danvers, MA), anti-RANTES (10R-R121A; Fitzgerald Industries International, Concord, MA), anti-MCP-1 (PA5-34505; ThermoFisher Scientific, Waltham, MA), and anti-F4/80 (MCA497GA, Bio-Rad, Hercules, CA). After incubation with primary antibodies at 4°C overnight, the slides were then stained with HRP-conjugated secondary antibody (Jackson ImmunoResearch Laboratories, West Grove, PA). Non-immune normal IgG was used to replace primary antibodies as a negative control, and no staining was visible. Slides were viewed under a Nikon Eclipse E600 microscope equipped with a digital camera (Melville, NY).

Immunofluorescence staining and confocal microscopy

Kidney cryosections were fixed with 3.7% paraformaldehyde for 15 min at room temperature. HKC-8 cells cultured on coverslips were fixed with cold methanol: acetone (1:1) for 10 min at -20°C. After blocking with 10% donkey serum for 1 hour, the slides were immunostained with primary antibodies against E-cadherin (# 3195), vimentin (#5741) (Cell Signaling Technology, Danvers, MA), E-cadherin (BD610181, BD Biosciences, Franklin Lakes, NJ), AQP1 (20333-1-AP, Proteintech, Rosemont, IL), c-met (sc-8057, Santa Cruz Biotechnology, Dallas, TX), AQP3 (SAB5200111), NCC (AB3553), fibronectin (F3648), laminin (L8271, Sigma Aldrich, St. Louis, MO), tPA (PT34, Oxford Biomedical Research, Rochester Hills, MI), TNC (ab6346, Abcam Inc., Cambridge, MA), and collagen type III (AB747; EMD Millipore, Burlington, MA). These slides were then stained with Alexa Fluor® 488 - or Cy3-conjugated secondary antibody (Jackson ImmunoResearch Laboratories, West Grove, PA). Slides were viewed under a Nikon Eclipse E600 microscope equipped with a digital camera or a Leica TCS-SL confocal microscope.

Kidney macrophage suspensions and flow cytometry assay

At sacrifice 10 days after IRI, kidneys were harvested from Lyz-met+/+ and Lyz-met−/− mice following perfusion with PBS. Kidneys were cut into small pieces and digested at 37°C in 1 mg/ml collagenase IV (Worthington) in complete RPMI for 30 minutes. Cells were filtered through 70 mm cell strainers and washed twice in PBS. The single-cell suspensions were slowly layered over 5 mL of Lymphocyte (Cedarlane). The tubes were spun for 1,300xg for 30 minutes at room temperature. The cell layer at the interface of the

media and Lymphocyte was collected and washed twice with PBS and used for FACS staining. To identify the macrophage population, cells were stained with fluorescent-conjugated antibodies CD11b (M1/70, #14-0112-82) and F4/80 (BM8, #14-4801-82, eBioscience™, ThermoFisher Scientific, Waltham, MA). Data were acquired on a BD LSRFortessa cytometer (BD Biosciences) and analyzed with FlowJo (Tree Star Inc.), as described previously (Ramani et al., 2018).

Isolation and culture of bone marrow-derived macrophages (BMDMs)

BMDMs were prepared as previously described (Na et al., 2016). In brief, bone marrow cells were isolated from femurs of C57BL/6J mice and cultured in RPMI 1640 medium, supplemented with 10% heat-inactivated FBS, 2 mM GlutaMax-1, 100 U/mL penicillin, 100 μg/mL streptomycin, and 25 ng/mL recombinant murine GM-CSF (#415-ML-010, R&D Systems, Minneapolis, MN) for 8-10 days with replacement of the medium every 2 days. Approximately 99% of the cells were F4/80+/CD11b+ when analyzed by flow cytometry. At day 8, BMDMs were treated with recombinant human HGF protein for another 1-3 days, and cells and supernatant were collected and subjected to analyses.

Western blot analysis

Kidney tissues were lysed with radioimmune precipitation assay (RIPA) buffer containing 1% NP-40, 0.1% SDS, 100 μg/mL PMSF, 1% protease inhibitor cocktail, and 1% phosphatase I and II inhibitor cocktail (Sigma) in PBS on ice. The supernatants were collected after centrifugation at 13,000×g at 4°C for 15 min. Protein expression was analyzed by western blot analysis as described previously. (Zhou et al., 2017) The primary antibodies used were: anti-vimentin (#5741), E-cadherin (#3195), anti-p-c-met (#3126), anti-GAPDH (#5174; Cell Signaling Technology; Danvers, MA), anti-TNC (ab6346; Abcam Inc., Cambridge, MA), anti-tPA (PT34; Oxford Biomedical Research, MI, USA), anti-uPA (17968-1-AP; Proteintech Group, Inc, IL, USA), anti-fibronectin (F3648), anti-α-SMA (A2547), anti-α-tubulin (T9026; Sigma Aldrich, St. Louis, MO), and anti-Actin (MAB1501; EMD Millipore, Burlington, MA).

Quantitative real-time reverse transcription PCR (qRT-PCR)

Total RNA isolation and qRT-PCR were carried out by procedures described previously (Fu et al., 2017). Briefly, the first-strand cDNA synthesis was carried out using a reverse transcription system kit according to the instructions of the manufacturer (Promega). qRT-PCR was performed on an ABI PRISM 7000 sequence detection system (Applied Biosystems, Foster City, CA). The mRNA levels of various genes were calculated after normalizing with β-actin. Primer sequences used for amplification are presented in Table S2.

QUANTIFICATION AND STATISTICAL ANALYSIS

All data were expressed as mean $\pm$ SEM if not specified otherwise in the legends. Statistical analysis of the data was performed using GraphPad Prism 9. Comparison between two groups was made using a two-tailed Student's t-test or the Rank Sum Test if data failed in normality test. Statistical significance for multiple groups was assessed by one-way or two-way ANOVA, followed by the Student-Newman-Keuls test. Results are presented in dot plots, with dots denoting individual values. Exact p values are presented for all dot plots. $p < 0.05$ was considered statistically significant.